ABSTRACT

Title of Dissertation:	MECHANICAL SIGNATURES OF BRILLOUIN SPECTROSCOPY
	Raymundo Rodríguez López, Doctor of Philosophy, 2024
Dissertation directed by:	Professor Giuliano Scarcelli, Fischell Department of Bioengineering

Brillouin light spectroscopy (BLS) has recently emerged as a tool for noncontact, nonperturbative and label-free characterization of biomechanical properties. BLS probes the longitudinal modulus of material while traditional techniques for biomechanical characterization aim to quantify Young's or shear modulus. However, empirical correlations between the different moduli have been observed in several biological materials, correlations that are not yet universally established. The objective of this thesis is to advance the understanding of these correlations and their limitations with controlled systematic comparisons of longitudinal modulus and gold-standard modulus of hydrogels and corneal tissue. First, using polymer hydrogels as model of study, experimental data and theoretical models were used to demonstrate that the correlation between longitudinal and shear moduli is due to their common dependence on underlying physico-chemical parameters of the polymer system. This dependence allowed to predict one modulus from the other when enough information of the system is available. Furthermore, the limitation of this

correlation was studied when hydrogels absorb water, finding that hydration affects both moduli but in different manner and thus, their correlation. Having established hydration as an important variable for biomechanical properties, the correlation between modulus in the corneal tissue and crosslinking procedure (CXL) was studied. CXL is the gold-standard treatment for corneal ectatic disorders, and its success is due to the strengthening of the mechanical properties of the cornea as a result of photochemical induced collagen crosslinking and dehydration of the tissue. However, most mechanical characterization *ex vivo*, does not factor in the tissue dehydration effect, overestimating the effect in the clinical situation. With experimental data obtained by gold-standard methods and established theoretical models, the modulus after hydration changes after the CXL was systematically characterized. Finally, another scenario where studying the correlation between moduli is important is the nonlinear mechanical behavior of the cornea. Effect that has been observed with different techniques, but BLS has failed to capture so far. This works proves that the reason of this discrepancy has to do with the mechanical anisotropy of the cornea and the nature of BLS, which is a purely uniaxial measurement of mechanical properties. Considering these factor, it is proven that BLS has the ability to measure the nonlinear mechanical properties of the corneal tissue.

MECHANICAL SIGNATURES OF BRILLOUIN SPECTROSCOPY

by

Raymundo Rodríguez López

Dissertation submitted to the Faculty of the Graduate School of the
University of Maryland, College Park, in partial fulfillment
of the requirements for the degree of
Doctor of Philosophy
2024

Advisory Committee:

Professor Giuliano Scarcelli, Chair
Professor Gregg Duncan
Professor Huang Chiao Huang
Professor Peter Kofinas
Professor Catherine K. Kuo

DEDICATION

Para mi familia, que me han apoyado sin dudarlo en cada momento de mi vida. No podría estar aquí sin tener en ellos a alguien a quien admirar y seguir, ni sin el incondicional amor que siempre me han brindado.

Para mis amigos, los nuevos que se han vuelto un grupo lleno de amor que nos cuidamos unos a otros; y los viejos que nos hemos visto crecer y siempre hemos estado uno para otro.

ACKNOWLEDGEMENTS

Thank you, Giuliano, for sharing the passion and knowledge about the research that you do, but thank you for also caring about the personal side of people. Thank you for always being available for anything I wanted to discuss and thank you for helping me grow not only as a scientist, but also in the human side with all the different conversations. I will always be grateful about the opportunity of working in your lab, where I have learnt a lot in the last 5 years, having experiences that I would never change for anything else.

I am also incredibly thankful to my labmates, who always were there available to discuss, to provide feedback and brainstorm solutions; but also to have fun, talk about our lives, grab some coffee and have a good laugh. I am sure this whole process would have been a lot more difficult without you. Thank you, Josh, Christina, Milos, Tony, Romanus, Maggie, Jake, Justin, Chenchen, Eric, Stephanie, Ivano. Thank you also to all the postdocs and to Jitao, who I also consider mentors and good friends, Hongyuan, Yoge, Jiarui, Claudia and specially Giulia. I want to specially thank Josh Webb, who guided me and mentored me at the beginning of my PhD research, you helped me a lot and I am very grateful that I could also come to you with any question, and you would help without any doubt. Thanks to Mete, who also taught me how to use instruments around the lab and was also another pair of eyes to discuss results and methods. Thank you Ana and Paco, who made my UMD experience a lot easier helping me to settle in and making everything in my life a lot easier.

Thank you very much to my Committee members, Dr. Catherine Kuo, Dr. Gregg Duncan, Dr. Peter Kofinas, Dr. Joe Huang, thank you for your time, interest in my work, and valuable

feedback during the proposal stage. Thank you very much to all the Professors that helped me through this process, to Dr. Helim Aranda, who was an initial contact and introduction to UMD; to Professor Fytas and Dr. Wang, whose infinitely knowledge helped to understand the importance of my research and helped me took my research to another level; to Dr. Peter Kofinas who also was always open to have a chat and to discuss results. I also want to say thank you to Dr. Sijie Hao and Dr. Christian Pick, who ran the Bioworkshop and taught me how to use several instruments. I also want to thank Professors form my Masters and Bachelor's degrees, Dr. Said Aranda, Dr. Vanesa Olivares, because I would not be here without everything they taught me at the beginning of this process.

Finally, thank you very much to my family and friends. There is nothing I could have achieved without your support, motivation, encouragement and love.

TABLE OF CONTENTS

LIST OF TABLES

LIST OF FIGURES

CHAPTER 1: INTRODUCTION

The goal of this thesis is to address a gap that exists when interpretating and comparing the Brillouin spectroscopy measured Longitudinal modulus (*M*) with the gold standard shear (*G*) and Young's (*E*) moduli in biomechanics.

Brillouin light scattering spectroscopy (BLS) has been demonstrated as a promising modality for biomechanical characterizations because it is an all-optical technique, and thus can provide noncontact, label and stain-free, and high-resolution 3D mapping of the elastic properties of cells and tissues.[1-5] However, BLS measures the longitudinal modulus (*M*) of materials at very high frequency (GHz), different from the gold standard methods that quantify Young's or shear elastic modulus in quasi static conditions (low frequencies <kHz). Despite such fundamental differences, gold-standard elastic moduli and longitudinal modulus have been empirically correlated for several materials of biological interests.[2,3,5,6] Yet, these empirical relationships are system dependent, and still need to be understood.

Chapter 3 is a fundamental investigation of the correlation between moduli. Polyacrylamide hydrogels are used as model systems for this study due to their ability to have their mechanical properties and their physico-chemical determinants finely tuned, controlled, and measured. Experimental data are analyzed and fitted to theoretical models of shear and longitudinal modulus to elucidate underlying principles of the correlations and the experimental conditions under which such correlation is valid.

In Chapter 4 an important phenomenon is investigated where the correlation between Brillouin modulus and Young's modulus would be of high significance: the corneal crosslinking procedure (CXL), the only procedure approved by the U.S Food and Drug Administration (FDA) to treat ectatic disorders.[7] The outcomes of the CXL include increase of modulus,[8-11] due to the induced crosslinks between the solid network of the tissue and dehydration of the tissue, which also affect mechanical properties.[12] The success of CXL in stopping ectasia progression is expected to be attributed to the increase of the mechanical properties of the cornea; however, hydration of the tissue has been shown to be a variable after the CXL procedure, with patients eventually returning to preoperative baseline levels over time.[13-14] Thus, the dehydration time-course and its effect on the modulus must be considered when measuring the mechanical effect of the CXL procedure. Hydration is one of the prominent factors identified in Chapter 3 that drives the correlation between Brillouin and Young's modulus. Therefore, the characterization and theoretical understanding of hydration-dependent modulus behavior after CXL is of critical importance. Previously, the dependency of Brillouin measurements on hydration and solid mechanical properties of the cornea was studied for virgin and CXL corneas based on a theoretical frame that describes the changes on the physiological characteristics of the cornea due to hydration.[15] But the same theoretical treatment has not been done before with mechanical testing.

Chapter 5 investigates the correlation between Brillouin and Young's modulus within the context of the classic non-linear mechanical behavior of the corneal tissue.[9] The intraocular pressure (IOP) is a constant force exerted on the cornea, inducing stresses in various directions within the tissue.[15] It has been demonstrated that changes of the modulus of the tissue occur in response to fluctuations in IOP, due to the cornea's nonlinear response.[17-21] Despite this, Brillouin

microscopy has not previously been able to detect any change in modulus induced by IOP-related stress.[20] This Chapter marks the first time in which the sensitivity of Brillouin microscopy to the nonlinear mechanical properties of the cornea is confirmed, and an investigation and comparison with gold standards measurements is also conducted.

CHAPTER 2: BACKGROUND

2.1 Moduli involved in biomechanics

Several biological processes are affected by mechanical properties at a fundamental level. From single molecules to living cells, and tissue growth, development and functionality all are affected by elasticity and viscosity.[22] The measurement of these elastic properties is commonly expressed in terms of elastic modulus, linking stress (force applied over a specific area) to strain (normalized deformation of the body), and having Pascals (Pa) as the measurement of unit.

Currently, the gold-standard to measure mechanics in biology is to measure the Young's and shear moduli, which provide a measurement of volume and density-conserving deformations. These moduli exhibit a strong frequency dependence, resulting in values typically expected in the kilopascal (kPa) range for low frequency deformations. However, for sufficiently high frequency measurements, the response is found in the gigapascal (GPa) range.[23,24] Other moduli that can be measured are the bulk and longitudinal moduli, however these are usually measured under different conditions since these involve volume and density changing high-frequency deformations (Figure 2.1).

In a formal definition, for an isotropic, elastic system, and under small deformations, the Young's (E) and shear (G) moduli are stiffness measurements that relate stress to strain. Stress is defined as load per unit area and has units of Pascals [Pa]; strain is defined as the deformation per unit length experienced in the direction of force, and it is unitless. Shear modulus (G) is the

resistance of a material to a transverse deformation and is defined as the ratio of the shear stress to shear strain:

$$G = \frac{shear\ stress}{shear\ strain} = \frac{{}^{F}/_{A}}{{}^{\Delta x}/_{l}} \quad \text{(Eqn. 2.1)}$$

Where F is the applied force, A is the force in which the force acts, Δx is the transverse displacement and l is the initial length. Shear modulus is usually measured with a rheometer, a device that studies the flow and deformation of materials under the influence of an external force applied by different plate geometries. To characterize materials such as hydrogels, that are inherently viscoelastic, dynamic oscillatory rheology is used to report quantitative measurements of viscoelasticity: storage and loss modulus, and ratio between them to measure damping abilities.

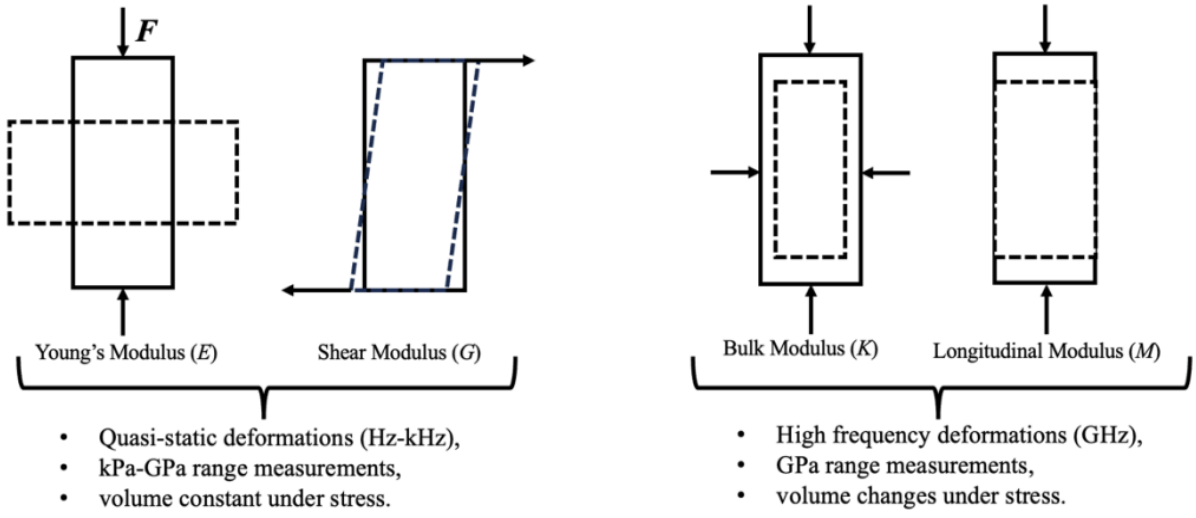

Figure 2. 1 Elastic moduli involved in biomechanics. Moduli can be generally divided into two groups, where we find the gold standard Young's and shear modulus with volume constant deformations; and the bulk and longitudinal modulus, with changing volume deformations. Even with these differences, empirical correlations have been found between the moduli.

Young's modulus (E) is defined as the ratio of tensile/compressive stress and axial strain.

$$E = \frac{tensile/compressive\ stress}{axial\ strain} = \frac{F/A}{\Delta l/l_0} \quad \text{(Eqn. 2.2)}$$

Where F is the applied force, A is the force in which the force acts, Δl is the length change (positive when sample is stretched, negative if compressed) and l_0 is the original length. Young's modulus can be measured with tensile or compression tests using a Dynamic Mechanical Analyzer (DMA). A DMA is a device that analyzes the materials response to controlled stress or strain, temperature, frequency, and gives information about the viscoelasticity of the material. Usually, these tests give as a result a stress-strain curve from where different compressive strain or stress values can be taken to analyze the modulus.

Young's and shear moduli can be related via the Poisson's ratio σ.[25]

$$G = \frac{E}{2*(1+\sigma)} \quad \text{(Eqn. 2.3)}$$

Poisson's ratio is a constant under small deformations, and it is defined by the ratio between the strain in the transverse to axial direction. For materials such as soft tissue, the Poisson's ratio~0.5, and the shear-Young's modulus relationship is simplified to

$$E = 3G \quad \text{(Eqn. 2.4)}$$

Bulk modulus (K) is defined as the ratio of pressure increase due to a decrease of volume, and it is formally defined as[25]

$$K = -V\frac{dP}{dV} \quad \text{(Eqn. 2.5)}$$

Where V is the initial volume of the sample and P is pressure. It can be experimentally measured by applying large quantities of stress while characterizing volume changes during deformation.[26] The bulk modulus can also be defined in terms of the Young's modulus (E) and the Poisson's ratio (σ):

$$K = \frac{E}{3*(1-2\sigma)} \quad \text{(Eqn. 2.6)}$$

Finally, the longitudinal modulus (*M*) is the ratio of axial strain to axial stress. It is a purely uniaxial measurement fundamentally different than the gold standard moduli. The deformation only occurs in one direction. It can be measured with the all-optical technique Brillouin Light Spectroscopy (BLS). Longitudinal modulus can be defined in terms of the Young's modulus (*E*) and the Poisson's ratio (σ): [27]

$$M = \frac{E*(1-\sigma)}{(1+\sigma)*(1-2\sigma)} \quad \text{(Eqn. 2.7)}$$

While all these moduli provide information of mechanical properties, and are fundamentally related, they rely on different physics. However, this description following elastic tensor, is for crystalline and solid materials, and biological tissue and cells do not strictly follow the straightforward relationship and rules of elastic solid. Therefore, it would be wrong to assume that the different moduli are directly proportional to each other. Moreover, most of soft tissues are considered viscoelastic material, with a Poisson's ratio ~0.5 and commonly called incompressible material[28]. This presents an issue because given the formal definitions, Bulk (*K*) and Longitudinal (*M*) moduli would approach infinity, requiring analysis to clarify this conflict between classic elastic equations and experimental data,[28] and to understand the previous empirical correlations in different biological samples.[2,3,5,6]

For these viscoelastic materials, *E* and *G* have a strong frequency dependence: with values expected in the kPa range at low frequencies, while for high frequency measurements it can reach GPa. Because volume of the sample is conserved when stress is applied, these contemplate changes along different planes of the sample. On the other hand, *M* and *K* are almost equivalent and in the GPa range. *M* measured with BLS, is in the GHz frequency range. When measuring *K* and *M*,

volume of the sample changes, in the radial direction and in a uniaxial direction, respectively. This means that BLS is highly directional and probes the mechanical properties only in the direction that is being tested.

2.2 Brillouin Light Spectroscopy (BLS).

Brillouin Light Spectroscopy is the technique to study the phenomenon of Brillouin light scattering, an inelastic scattering of light by spontaneous acoustic waves intrinsic to matter. This phenomenon was first observed in the 1920s by Leon Brillouin,[29] but it was until the 1960s when laser light sources became easily available and several improvements in Fabry-Perot interferometers allowed to use this technique to study materials[30-33] and different biologically samples *ex vivo*, such as collagen fibers,[34-35] bone,[36] lens and cornea[37-38] of different animals. Later, with the use of Virtually imaged phased array (VIPA)[39,40] spectrometers, the acquisition time of a single spectrum was reduced, and in combination with a confocal microscope studies have been conducted at cellular and tissue levels exploring mechanical cues.[2]

In BLS, the dynamics of the spontaneous acoustic waves in matter, also known as acoustic phonons, induce fluctuations in the refractive index of a sample. These fluctuations are reflected in the spectrum of the scattered light, which experiences a Doppler frequency shift, also referred as the Brillouin frequency shift (Figure 2.2A). Simultaneously, the dynamics of these phonons are dictated by the viscoelastic properties of the material. Therefore, the Brillouin spectrum provides insights into the elastic properties of the material on a uniaxial microscale.[33]

A Brillouin spectrum typically shows an intense central peak due to Rayleigh scattering and shifted peaks, representing the Stokes and anti-Stokes frequency shifts (Figure 2.2B).[41]

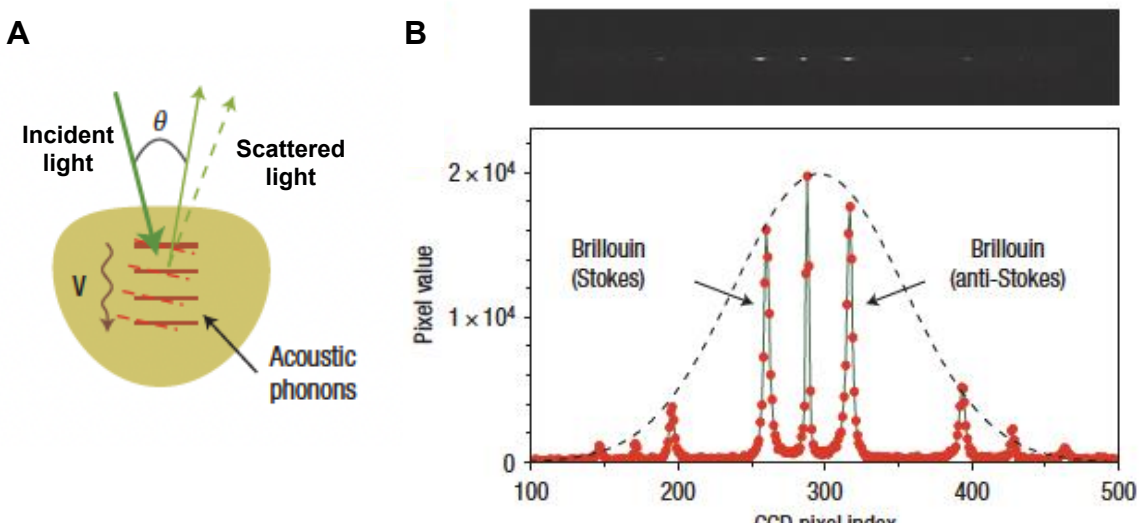

Figure 2. 2 A. Illustration of the Brillouin scattered light after interacting with the acoustic phonon. Figure 2.2 B . Typical Brillouin spectrum with a CCD camera. In this case of distilled water, showing the intense peak in the center of Rayleigh scattering and the Stokes and anti-Stokes Brillouin peaks. Adapted with permission [41].

The Brillouin shifts relative to the elastic peak (ω_B) are related to the acoustic wave velocity (V) in the material, and the momentum exchanged in the scattering process (q):

$$\omega_B = \pm Vq \qquad \text{(Eqn. 2.8)}$$

The momentum q, is defined as

$$q = \frac{2n}{\lambda_i} sin\frac{\theta}{2} \qquad \text{(Eqn. 2.9)}$$

where n is the refractive index of the material, θ is the scattering angle and λ_i is the incident light wavelength in vacuum. A typical configuration for Brillouin applications use a backscattering geometry (θ= 180°), where q simplifies to

$$q = \frac{2n}{\lambda_i} \qquad \text{(Eqn. 2.10)}$$

With these equations, the Brillouin frequency shift peaks are described:

$$\omega_B = \pm V \frac{2n}{\lambda_i} \quad \text{(Eqn. 2.11)}$$

With another approach, Longitudinal modulus (M) depends on the density of the material (ρ) and the square of the velocity of the acoustic wave of the material (V):

$$M = \rho V^2 \quad \text{(Eqn. 2.12)}$$

$$V = \sqrt{\frac{M}{\rho}} \quad \text{(Eqn. 2.13)}$$

Allowing to obtain relevant information on the elastic properties of the material from the spectral shift with Equations 2.11 and 2.13.

$$\omega_B = \pm \frac{2n}{\lambda_i} \sqrt{\frac{M}{\rho}} \quad \text{(Eqn. 2.14)}$$

$$M = \rho \frac{\omega_B^2 \lambda_i^2}{4n^2} \quad \text{(Eqn. 2.15)}$$

provided that the ratio $\frac{\rho}{n^2}$ is independently measured, and it has a very small variation within cells and tissue.[1,2] In this way, BLS mechanical properties of samples can be measured via the longitudinal modulus and its relationship with the scattered light.

In our laboratory, and the work conducted in this thesis, a Brillouin microscopy setup with a two VIPA spectrometer[40] is used (Figure 2.3). In the setup, a 660 nm continuous wave laser (Torus, Laser Quantum) is focused into the sample by an objective lens and the backscattered light is collected through the same objective and coupled into the Brillouin spectrometer. A built-in house program (LabVIEW) is used to control the translational stage where the sample is placed, and the image acquisition (EMCCD Andor camera). These allowed to control the region of interest of the sample, scanning step size and exposure time of the scan. Water and ethanol, materials with known Brillouin shifts are used to calibrate the Brillouin microscopy set up before measurements. Post-processing is done with a MATLAB algorithm where the Brillouin peaks are fitted to a Lorentzian function to calculate the Brillouin frequency shift per pixel.

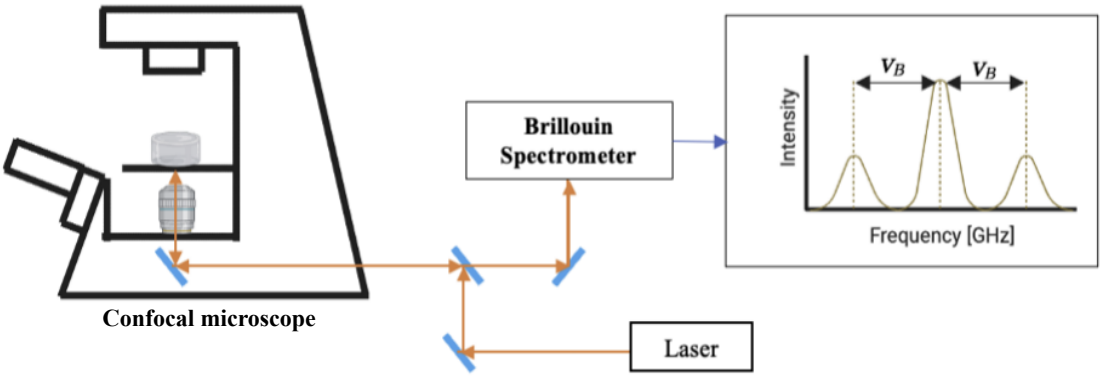

Figure 2. 3 Illustration of the Brillouin microscopy setup.

2.3 Polyacrylamide hydrogels.

The first model system studied in this thesis for Chapter 3 are polyacrylamide hydrogels. This model was chosen because by varying the polymer fraction of the hydrogel and the crosslinking density, the mechanical properties of the hydrogel can be easily manipulated.[42,43] Hydrogels have been an object of study for Brillouin technology before, however these have been

used to study the effect of concentration of polymer,[44] the temperature,[45] the linewidth of the Brillouin spectra,[46,47] or the effect at highly hydrated conditions;[48] and not to elucidate the correlation between the Brillouin measured longitudinal modulus and the Gold standard shear modulus, based on a theoretical background.

Hydrogels were prepared with acrylamide as monomer, N'N' methylene bis-acrylamide as crosslinker and DI water at room temperature. The bis-acrylamide formas a chemical crosslink between neighboring acrylamide chains, growing in a three dimensional network. Three different conditions were prepared (neutral, positively charged, and an alternative initiator hydrogel) to induce chemical structural differences, while maintaining familiarity between the samples. The samples were also used in two different equilibrium states: the relaxed state just after polymerization, and the swollen-to-equilibrium state, where the equalization of the osmotic and elastic forces lead to a different strand conformation.[49]

2.4 Corneal architecture.

Chapter 4 and 5 use the corneal tissue as the object of study. The cornea is a transparent avascular tissue, it is the outermost transparent layer of the eye and acts as a structural protection barrier and contributes to the refractive power of the eye.[50] The cornea is made up of cellular (epithelial and endothelial cells, keratocytes) and acellular components (collagen, proteoglycans and glycosaminoglycans).[51-54] The human cornea is approximately 550 μm, and it is divided into five different layers, from anterior to posterior: epithelium (~45 μm), Bowman's layer (~15 μm), stroma (~500 μm), Descement's membrane (~10 μm), and endothelium (~5 μm).[52,55,56] The epithelium layer acts as a protective layer that maintains hydration;[56] Bowman's and Descement's

membranes act as protective layers to the adjacent layers;[57,58] the stroma represents ~80-90% of corneal thickness and is the main component to account for biomechanics;[59,60] and the endothelium serves a function of active transportation of water between the cornea and the anterior chamber of the eye[61] (Figure 2.4). It is important to notice that some mammals, including pigs (sample of study in this thesis), the Bowman's layer is not present.[62,63] However, due to the biological and morphological similarities with the human cornea, it represents a good model for clinical and non-clinical purposes.[64]

The corneal stroma has a specific architecture that provides unique characteristics for the transparency and appropriate curvature of the cornea to transmit and refract light for an acute vision. And representing most of the corneal tissue, the stroma is the main component for biomechanics of the tissue. This layer consists of collagen type I, II, V and VI, found in the triple helix structure;[65] the collagen is arranged into highly organized fibrils with uniform spacing and alignment crucial for transparency. The diameter of these collagen fibrils range from 22.5 nm to 35nm, depending on collagen type.[66] The fibrils are packed into layers called lamellae, which are stacked on top of each other, each oriented in an orthogonal direction to adjacent lamellae, important for corneal strength[52] (Figure 2.4). This also means that the cornea is an anisotropic tissue, with a different configuration, and thus different biomechanical behavior, in the radial direction and in the tangential direction of the tissue.

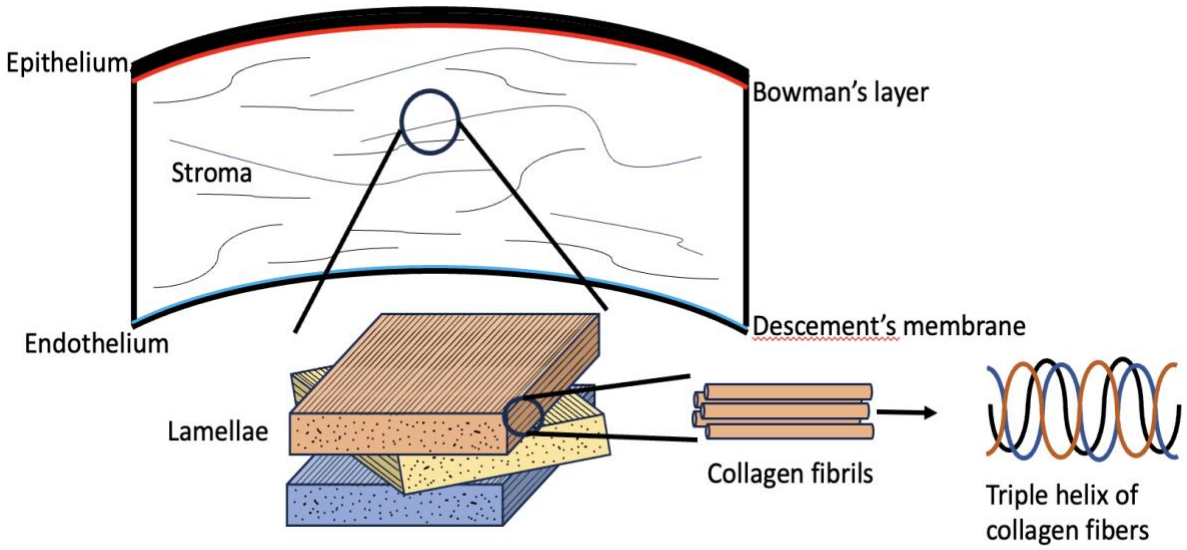

Figure 2. 4 Diagram of the architecture of the corneal tissue. Layers of the cornea and collagen organization are illustrated.

Furthermore, the corneal stroma also presents a special architecture that is depth dependent from the surface. Collagen fibrils in the anterior stroma present a more disorganized and interweaving behavior within each other compared to the posterior stroma where is considered a more organized and hydrated system.[67-70] This specific conformation gives the anterior part of the stroma stiffer mechanical properties[70-73] and resistance to swelling when the whole corneoscleral tissue is uncorrupted.[69]

2.5 Biomechanical properties of the cornea.

Soft biological tissues, including the cornea, have a typical non-linear stress-strain relationship.[12,74] When doing a biomechanical characterization, it is important to define the type of modulus and the level of strain or stress in which calculations or experiments are done in the nonlinear mechanical curve. A common modulus to report, and the one that will be reported in this thesis, is the tangent or Young's modulus (E), which is the slope of the stress/strain curve. However, the calculated modulus can change according to the specific stress or strain that is being measured i.e. the modulus will increase as the strain or stress increases. When a typical J-shaped curve is observed on a collagenous soft tissue, there is usually a linear region at very low strains known as the toe region; followed by a region where there is an evident change of modulus with strain, known as the heel region; and finally a more linear relationship at higher strains, which is maintained until failure (Figure 2.5).[60]

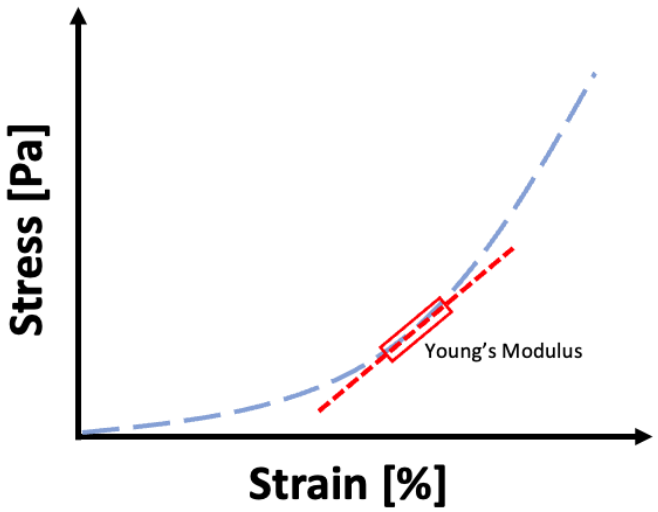

Figure 2. 5 Typical nonlinear stress-strain curve for a soft tissue. The Young's modulus is the slope of the of the curve at a specific stress/strain.

These nonlinear stress-strain curve for corneal tissue in a uniaxial tensile test is explained by the collagen organization: at the toe region there is uncrimping of the collagen molecules, followed by the removal of microscopic kinks in the heel region, and finally the sliding of collagen molecules past one another at the linear region.[75-77]

As explained before, the cornea is physically an anisotropic material resulting in significantly differences of the mechanical properties based on the probing direction of the mechanical test. Due to the collagen organization and alignment, the corneal stiffness in the tangential direction (parallel to the surface of the cornea) is considerably higher than the compressive stiffness through the thickness of the cornea.[60] It has been reported that compressive stiffness is two orders of magnitude smaller than the tensile stiffness.[78] This also can be related to the rule of mixtures, and in the case of the cornea, a fiber reinforced composite.[79] The rule of mixtures presents the case that the components of a mix will add their modulus of elasticity in a linear form, adding the modulus affected by the volume fraction of each component,

$$E = f_m E_m + f_f E_f \qquad \text{(Eqn. 2.16)}$$

with the subscripts *m* and *f* refer to matrix and fibers, respectively. Conversely, the inverse rule of mixtures is the situation in which the modulus of each component is independent of each other and it is weighted by their volume fraction, making this lower than when the moduli add in a linear way.

$$\frac{1}{E} = \frac{f_m}{E_m} + \frac{f_f}{E_f} \qquad \text{(Eqn. 2.17)}$$

For the case of the cornea, the linear case would be observed when the load is applied in the same direction as the fibers. And the second case would be when the modulus is applied in a

perpendicular direction to the fibers. This explains the difference of modulus observed in the radial and tangential direction of the cornea, which can be up to two orders of magnitude.[74]

The corneal tissue is under constant stress and strain in multiple directions by both intraocular (intraocular pressure IOP) and extraocular (eye rubbing, blinking) forces. But the cornea has mechanisms to regulate and distribute these stresses in a manner that maintains adequate for stable vision, mostly continuous pumping changing hydration state biomechanics.[60] The intraocular pressure (IOP) is a constant force with minimal variation according to activities during the day.[80] In healthy humans the IOP varies from 12-20 mmHg, but in abnormal conditions, such as glaucoma, the IOP can reach up to 70 mmHg.[81] These changes in the IOP are reflected in the general stiffness of the cornea due to its nonlinear mechanical behavior. Effect that has been proved before with load-displacement indentation methods,[82] optical elastography techniques[17-20] and simulations.[19,83] Chapter 5 of this thesis will also prove this effect with porcine corneas *ex vivo* using BLS, method that had failed to prove this before.

Another factor that affects biomechanical properties of tissues is the hydration level. Previous studies have investigated the correlation between the biomechanical properties of the cornea and its hydration level, demonstrating that as hydration in the tissue increases, the overall biomechanical strength decreases.[9-11] The general consensus from these studies suggests that not considering hydration when measuring biomechanical properties might lead to inaccurate results. Chapter 3 of this thesis studies this relationship of mechanical properties of the cornea and hydration, in control cases and after the crosslinking procedure.

2.6 Corneal ectatic disorders and crosslinking.

Corneal ectatic disorders are distinguished by distortion of the corneal curvature, which is usually associated with a mechanically speaking "weaker" cornea.[84] This is thought to be the result of aberrant collagen organization,[85] loss of anchoring collagen fibrils and stromal thinning.[86] Keratoconus is the most prevalent ectatic disorder. It is a noninflammatory progressive condition in which the cornea gets thinner and steeper over time, resulting in blurry and distorted vision; and if left untreated, it can result in more damage to the cornea and complete loss of functional vision.[87]

Keratoconus is morphologically characterized by the bulging or coning of the corneal surface, and 97% of the keratoconus cases are located in the central and paracentral regions.[88] Thus, keratometry is a marker of severity of the keratoconus condition: values of 46 diopters should be considered as a sign of mild or initial keratoconus, and an advanced condition when the curvature is >53 diopters.[88] Topography and tomography techniques have been used to evaluate the severity of the condition, usually being evident in the later stages; however, due to the alterations of the local biomechanical properties of the corneal tissue, recent studies have been focusing in measuring these biomechanical properties, as another marker that has shown better sensitivity and the ability to detect early stages of the keratoconus condition.[89-92]

The management for the keratoconus condition was restricted to spectacles, rigid contact lens and corneal transplant, until the late 1990's, where the idea of increasing the stiffness of the corneal tissue to stop the development and progression of the condition started to be studied.[93-94] In 2003, a protocol for corneal crosslinking (CXL) was established and successfully performed *in vivo*: the Dresden protocol, a procedure that has been clinically used world wide, but only until

2016 FDA approved in the US as treatment of the keratoconus.[7,95] The approved CXL procedure involves the removal of the epithelium layer of the cornea to soak the stromal layer in a photosensitizer solution of 0.1% Riboflavin and 20% Dextran for 30 minutes, followed by UV-A light exposure of 3mW/cm^2 for another 30 min and a total of 5.4 J/cm^2, applying riboflavin solution continuously in 3-5 minutes intervals.[7] In the solution, the riboflavin acts as a photosensitizer that absorbs UV-A light energy to induce covalent bonds between collagen molecules;[8] the polysaccharide Dextran was originally introduced to prevent swelling of the corneal tissue due to the osmotic difference, potentially affecting the procedure. However, the accepted CXL protocol actually results in loss of water content, as observed by the thickness-hydration relationship[12,96] and the thinning of the corneal tissue[13,97] post-procedure. This is an important step in the procedure because it has been proved that mechanical properties are affected by the hydration of the tissue: an increase in water content leads to a decrease in the overall tissue stiffness.[9-11] This effect will be studied in Chapter 4 of this thesis. Yet, the hydration of the tissue *in vivo* is a variable that changes over time, and although there is dehydration after the CXL procedure, this level is recovered after a certain period, returning the corneal tissue hydration to baseline preoperative levels, while maintaining the visual improvement of the patient.[13,14]

The reaction of CXL between the riboflavin and UVA light occurs in a photo-oxidative manner, and although there are still questions to be answered about the mechanism of the CXL, experimental data suggests that it is a mixture of both aerobic (Type 2) and anaerobic (Type 1) reactions.[98,99] At an early stage of the procedure there is ground-state oxygen available which reacts with the excited riboflavin molecule in its triplet state, producing reactive oxygen species (ROS), a type 2 reaction that last around 15 seconds. Once the oxygen is consumed, a type 1

reaction starts, where the riboflavin triplet state reacts directly proteins in the stroma, generating ROS. These ROS, created as byproducts, mediate the formation of crosslinks by reacting with available groups nearby, usually of collagen fibrils and proteoglycans, promoting the crosslinking between neighboring molecules.[98,99] Replenishment of oxygen occurs naturally as the UVA irradiation is discontinued, promoting again Type 2 reactions.[99]

The standard Dresden protocol is time consuming and can be uncomfortable for the patient, so there is an effort to find alternative protocols, including methods without the removal (or a partial removal) of the epithelium, and faster options with higher UVA light fluence and reduced exposure time to maintain a constant total irradiance known as Accelerated Crosslinking (accCXL).[98] However, the efficiency of these techniques remains unsuccessful when compared to the Dresden protocol, probably due to lower absorption of the riboflavin in case of the epithelium-on case; and mixed results that do not support accCXL in clinical settings suggesting a reduction of the stiffening effect on the corneal tissue.[98,99]

The results and effects of the CXL treatment rely on *ex vivo* data and clinical follow ups evaluating the effectiveness of the procedure on the patients. This is one of the reasons why the treatment first published on 2003 was not approved in the US until 2016.[7,95] The lack of an effective biomechanical characterization of the cornea *in vivo*, and the differences of hydration and stiffness that the tissue might suffer during the CXL procedure and certain time post-operation, prevents us from a real quantitative estimation of the CXL effect on the corneal tissue.

CHAPTER 3: NETWORK VISCOELASTICITY FROM BRILLOUIN MICROSCOPY*.

3.1 Introduction.

This chapter reports a fundamental investigation for a correlation between the Brillouin measured longitudinal modulus and the gold-standard shear modulus measured with typical methods. This observed correlation is only empirical and system dependent but of fundamental interest and immense practical value in biomedicine due to the importance of shear modulus and the possibility to map the longitudinal modulus at high-resolution with all-optical spectroscopy. In this chapter we investigate the origin of such correlation in polyacrylamide hydrogels as models of controlled samples with tunable mechanical properties. Experimental data and theoretical models for both moduli are used to establish the conditions and limitations of the empirically observed correlations.

Biomechanical characterizations are traditionally performed by quantifying the Young's (E) and shear (G) moduli in quasi static conditions (low frequencies < kHz). However, the techniques to measure these moduli usually require contact forces (atomic force microscopy,[100] micropipette aspiration,[100] microrheology[102]) or lack resolution for a subcellular mapping in 3D (optical coherence elastography,[103] ultrasound,[104] magnetic resonance imaging[105]). Elastic moduli also have a strong frequency dependence with values expected in the kPa range at low frequencies. For sufficiently high frequency measurements, where the stress is applied fast enough to prevent the system from relaxing, the viscoelastic response of incompressible materials is found in the

* The results on this Chapter were part of a peer-reviewed publication, Rodríguez-López et al. *Biomac* 2024;*25*(2): 955-963.

MPa-GPa range.[106,107] This would also mean that when comparing two given mechanically different hydrogels (one stiffer than the other), at low frequency variations the modulus could vary by about orders of magnitude (from a few kHz to 0.1 MHz); whereas at GHz frequencies, the modulus is about a few hundred MPa, with a much smaller variation (~30%) over the same composition range. Figure 3.1 is an illustration of the investigation in this chapter, a possible relationship between the modulus measured at different frequencies and that come from different physical reasons. In recent years, Brillouin light spectroscopy (BLS) has been demonstrated as a promising modality for biomechanical characterizations because it is all-optical, and thus can provide noncontact, label-free, and high-resolution 3D mapping of the elastic properties of cells and tissues.[1-5] However, BLS measures the longitudinal modulus (M) of materials at hypersonic frequencies (GHz). Despite such fundamental differences, Young's/shear and longitudinal moduli have been empirically correlated for several materials of biological interests, such as corneal[5] and lens[1] tissue, cells,[2] or gelatin gels.[6] The reason of this empirical correlation is a question that remains open in the field, and work is being done to understand if there is a fundamental reason behind the relationship between the elastic modulus measured at low frequencies and elastic modulus measured at low frequencies and elastic modulus measured at high frequencies in different systems.

The hypothesis for this observed correlation is that it originates from a common dependance of both moduli on the same underlying physico-chemical properties.[2] To elucidate the physical origin of the empirical correlation between shear and longitudinal moduli, polyacrylamide hydrogels (AA) with polymer volume fractions in the range of 5-20% were used as model systems. With this investigation it was demonstrated that both moduli depend on the local segmental

packing of the hydrogels, expressed in an effective gel composition as the volume fraction that the polymer occupies in the hydrogel. This parameter depends on different characteristics of the hydrogel, such as the polymer-solvent interaction, water content and crosslink density. For these AA samples, the polymer volume fraction (ϕ) was estimated experimentally, and a theoretical analysis was used to explain the dependence of the experimental shear and longitudinal modulus.

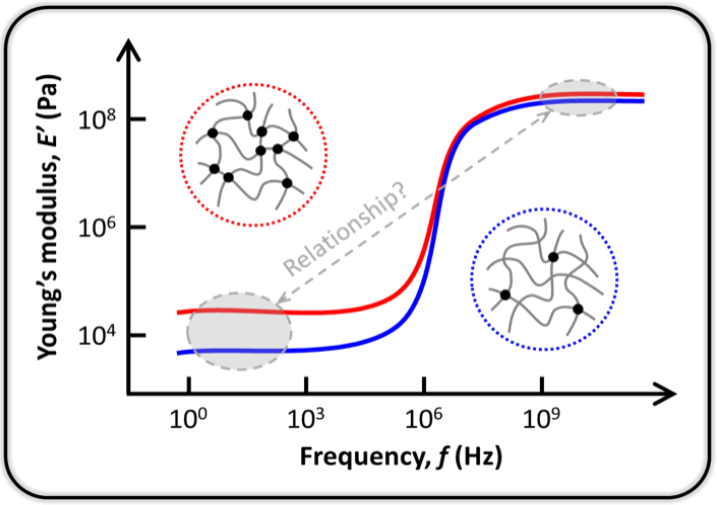

Figure 3. 1 Schematic illustration of the frequency dependence of the elastic modulus in two mechanically different hydrogels (one stiffer than the other) and if there is a correlation at the different frequencies and measured moduli.

For shear modulus G, the expected strong ϕ-dependence is rationalized by an effective volume fraction (ϕ_{eff}) based on the scaling theory of polymer networks that accounts for monomer-solvent interactions. In the case of the longitudinal modulus M, there is a much weaker ϕ-dependence due to absence of polymer chain effects and it is expected that the material obeys the rule of mixtures.[108] The inverse rule of mixtures was found to represent the experimental $M(\phi)$ of the AA in agreement with the $M(\phi)$ of physical AA networks. Based on these considerations, the correlation between shear and longitudinal moduli was explained with a theoretical background of both moduli, and experimentally verified it with hydrogels prepared at three different conditions

(neutral, positively charged, and an alternative initiator hydrogel) with tunable mechanical properties (by varying the crosslinker and polymer concentrations).

To study the limitations of the correlation, the AA hydrogels but swollen-to-equilibrium, where the equalization of the osmotic and elastic forces leads to different gel strand conformation.[49] The same workflow was applied to these hydrogels to analyze any correlation, finding that in this scenario the shear and longitudinal moduli are affected differently by the swelling ratio, which represents the amount of water that entered the hydrogel; as a result, important corrections to the empirical correlations must be applied.

3.1.1 Mechanical characterization of hydrogels with Brillouin Light Spectroscopy (BLS).

BLS has been previously used to study the viscoelastic characteristics of hydrogels and some of the variables that affect them, such as polymer volume fraction,[109,110] temperature dependence,[111,112] and crosslinking density.[113] These studies showed that the longitudinal modulus can be affected by these intrinsic properties of the hydrogel, but without a comparison to any other viscoelastic characterization. On the other hand, different molecular weight PDMS hydrogels have been used to characterize the viscoelastic properties at low and high frequencies, using rheometry and ultrasonic techniques to measure shear and longitudinal moduli, respectively.[114] Shear and longitudinal moduli (measured by BLS) have been measured and correlated for hydrogels before, using gelatine[6] and polyacrylamide;[2] or polyethylene oxide gels.[48] However, these studies only show an empiric correlation as a validation of the changes of viscoelastic characteristics of the hydrogel;[2,6] or use highly hydrated hydrogels as object of study, where water content (>90%) strongly affects BLS measurements.[48] The aim of this Chapter is to investigate the underlying

reasons behind such correlations with theoretical and experimental evidence on polymer model systems; in the process, it is quantitatively establish the material and experimental conditions, under which the correlation between the two moduli is valid or needs additional information. Furthermore, compared to previous studies, a wider percentage of water is covered, starting from highly hydrated hydrogels with more than 95% water content to samples ~75% water content, a value closer to physiological conditions of tissue[115] and cells.[116]

3.2 Materials and methods.

3.2.1 Preparation of hydrogels.

All chemicals used for the hydrogel synthesis were purchased from Sigma-Aldrich. Stock solutions w/v of 40% acrylamide as monomer, and 2% N'N' methylene bis acrylamide as crosslinker, were prepared with DI water at room temperature, and used with the desired amount of initial polymer volume fraction of monomer and crosslinker for different stiffness values.[43] Tetramethylethylenediamine (TEMED) and a 10% ammonium persulfate (APS) solution prepared fresh were used as initiators for the neutral and charged gels. Hydrogen peroxide and temperature were used as initiators in the alternative initiator hydrogel option,[117-118] following a protocol to form low molecular weight polyacrylamide chains. 3-methacrylamidopropyltrimethylammonium chloride (MAPTAC) was used as the cationic monomer in the charged gels.[119]

For these experiments, a mixture of the desired amount of monomer and crosslinker were mixed with DI water to obtain an initial monomer concentrations of 5%, 7.5%, 10%, 15% and 20%; each at four different crosslinking agent concentrations (ratio crosslinker 1:polymer= 1: x, with x = [30, 25, 20, 10]). Afterwards, TEMED was added carefully into the mix (4 μl per ml),

and lastly, APS solution was added into the mix (6 μl per ml).[43] For the charged gels, 1% of the MAPTAC was added to the mix, and considered for the desired amount of monomer calculation. For these hydrogels, the pH level was adjusted with 0.1 M NAOH or 0.1 M HCl to pH7 to allow polymerization.[119] In the alternative initiator hydrogel, the mix was prepared in the same way as the neutral hydrogels, but the polymerization was carried out by adding 10 μl per ml of hydrogen peroxide and placing the mold in a temperature bath at 70°C until polymerization was completed (adapted from refs 117,118). For all hydrogels, the mix was poured into a mold to obtain a flat layer of hydrogel (<2cm), and after letting the mix rest for 30 minutes to ensure full polymerization, a 5 mm diameter disk was cut and immediately used for measurements. If hydrogels were not used at the moment, they were maintained in a sealed mold to avoid gain or loss of water due to the environment. Hydrogels were used in three different states: just after polymerization "relaxed state"; after swelling to equilibrium "swollen state"; and after leaving the hydrogels to completely dry "dry state". Mass of the hydrogel for the "relaxed state" W_r was measured just before the mechanical measurements. The "swollen state" hydrogels were obtained by immersing the hydrogel in DI water for 48 hours, until the maximum amount of water was absorbed, and the mass of the hydrogel did not change anymore. Mass of the hydrogel in "swollen state" W_s was weighted. Afterwards, the samples were left to dehydrate for >48 hours, until only the polymer fraction was left (dry state) and weighted again to obtain W_d. The volume fraction of polymer of the swollen hydrogels was calculated

$$\phi_S = \frac{V_d}{V_s} \qquad \text{(Eqn. 3.1)}$$

obtained from the volume of the swollen gels, V_s. In view of the tiny amount of crosslinkers, they were neglected in the volume fraction calculations.

3.2.2 Shear rheology.

The shear modulus G was measured by rheometry (TA Ares-G2 rheometer) with an 8 mm diameter parallel plate, adding sandpaper to the parallel plate to prevent the sample from slipping. A frequency sweep in the range of 0.1-10 Hz was performed in the linear viscoelastic region, taking the value of the storage shear modulus at 1Hz and at 1% strain at 25℃.[1] All the values reported for shear modulus are the elastic or storage modulus G', since this value is significantly greater than the loss modulus G'' in this elastic region. The subscripts refer to the state of the hydrogel, G_r for relaxed hydrogels and G_S for swollen hydrogels.

3.2.3 Brillouin Light Spectroscopy (BLS).

BLS was used to calculate the longitudinal modulus of the hydrogels, measuring the Brillouin shift derived of the different hydrogels and using Equation 2.15. Where the values of n and ρ are the refractive index [n=1.45 for monomer acrylamide[120]] and the density of the material [$\rho_p = 1.13$ g/cm^3 for monomer acrylamide[121]].

The Brillouin microscopy set up described in the *CHAPTER* **2:** BACKGROUND section was used to measure the frequency shift. For these experiments, a 660 nm continuous wave laser (Torus, Laser Quantum) with a power ~30mW was focused onto the sample by an objective lens (40X/0.6NA, Olympus), with a transverse resolution of ~0.4 μm and an axial resolution of ~2.6 μm. The sample was placed and a cross-section image of the center of the hydrogel was imaged in a XZ plane, obtaining an image with an X displacement of 500 μm and the entire hydrogel in Z representing the Brillouin shift of the hydrogels. An average of the whole scan was chosen as the representative value of the Brillouin shift for the measured hydrogel. The resolution of the image

was chosen to be 20x50 μm per pixel; the image acquisition (EMCCD Andor camera) was performed with an exposure time of 50 ms.

3.3 Results and discussion.

3.3.1 Relaxed hydrogels.

Longitudinal and shear moduli were measured for the different AA hydrogels in a "relaxed state", which means just after polymerization and without any drying or swelling. The different hydrogels are labelled in the different figures with these code through this chapter: neutral charged gels (●), 1% cationic charged gels (▲) and low molecular weight hydrogels (★). The initial monomer concentration is labelled with color code: 5% (black), 7.5% (green), 10% (blue), 15% (light blue) and 20% (red) monomer; and each at four different crosslinking agent concentrations (ratio crosslinker 1:polymer= 1: x, with x = [30, 25, 20, 10]) as represented by the distinct data points. For the 15% and 20% hydrogels, only the 3 lower crosslinker ratios were used, since the higher crosslink ratios led to opaque hydrogels. All investigated hydrogels were clear and completely polymerized for measurements.

The nominal polymer volume fraction of the hydrogels ϕ (i.e., water content) was calculated as:

$$\phi = \frac{V_d}{V_r} = \left(1 + \frac{\rho_p}{\rho_s}\left(\frac{W_r}{W_d}\right) - \frac{\rho_p}{\rho_s}\right) \qquad \text{(Eqn. 3.2)}$$

where V_d and V_r are the volume of the dry and relaxed gels; ρ_p and ρ_s are the density of the polymer and the solvent (water in this case); and W_r and W_d are the mass of the gels in the relaxed and dry state ($V_r = \frac{W_r}{\rho_r}$, where $\rho_r = \rho_s(1-\phi) + \rho_p \phi$). All the samples were weighted in the

relaxed state (W_r), and their longitudinal and shear moduli were measured right after. The results were plotted in a log-log form, shear modulus of the relaxed hydrogels G_r vs the nominal polymer fraction ϕ (Eqn. 3.2) in Fig. 3.2A, where an overall scaling behavior (i.e., $G_r \sim \phi^{\alpha}$) with a slope α~2.2±0.1 is observed and represented with a solid black line, R^2=0.85. Separating the samples in labelled neutral charged gels (●), 1% cationic charged gels (▲) and low molecular weight hydrogels (★), the slope a will increase from 2 to 2.5. The longitudinal modulus of relaxed hydrogels M_r is also plotted against ϕ and represented in Figure 3.2B. In this case, the inverse rule of mixtures Equation 2.17, is applied for the hydrogels

$$\frac{1}{M_r} = \frac{1-\phi}{M_w} + \frac{\phi}{M_p} \qquad \text{(Eqn. 3.3)}$$

where M_w=2.22 GPa is the longitudinal modulus of water and M_P=16.35GPa[48] is the longitudinal modulus of the pure polymer, and it is represented by the blue dashed line. The inverse rule of mixtures is found to represent the data in contrast to the linear rule of mixtures ($M_r = \phi M_p + (1-\phi)M_w$) represented with the red dotted line.

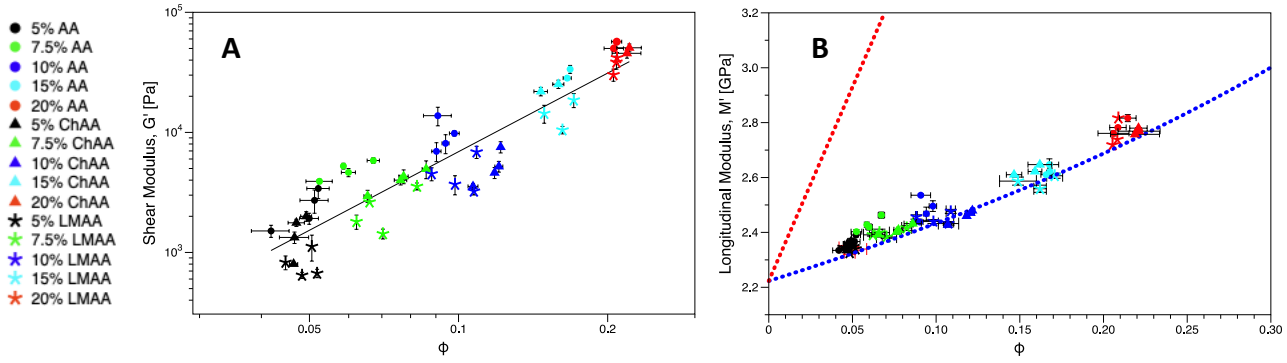

Figure 3. 2 A. Log-log plot of shear modulus G_r vs experimental polymer volume fraction ϕ of AA hydrogels in relaxed state. B. Longitudinal modulus M_r vs experimental polymer volume fraction ϕ of the same hydrogels. In both A and B, the data points are scattered for the different crosslinking agent contents at a constant AA concentration.

Among all studied samples, M_r in GPa changes by ~21%, whereas the corresponding change in G_r, falling in the kPa range, amounts to ~88 times. This indicates a much weaker variation in M_r than G_r, due to the much stronger volume fraction dependence of the latter. However, significant scattering around the fitting lines is observed in both $G_r(\phi)$ and $M_r(\phi)$. Although care was taken to ensure that measurements were done immediately after polymerization, there might be variability in water content - in a higher humidity day water enters through the atmosphere into the gel, whereas on a drier day the water in the gel may evaporate. Therefore, the water content in any state, particularly the "relaxed" state which is not an equilibrium state may differ from the expected value. Since the experimental uncertainties of both moduli cannot account for the large deviations, the water content of the samples probably does not represent the driver of either hydrogel moduli. Indeed, when measuring ϕ, only the density and weight of the elements of the mix are considered but to correctly evaluate the material response, other parameters such as the polymer-solvent interaction or crosslink density should also be taken into account.[122]

Theoretical frame for measured moduli in hydrogels.

To correctly estimate an effective volume fraction (ϕ_{eff}), Rubber Elasticity Theory (RET) and the scaling concepts of semi-dilute polymer solutions are used. This ϕ_{eff} which considers the polymer/solvent interaction and crosslink density. According to RET the shear modulus G is defined as:[123,124]

$$G = \frac{kT}{\xi^3} \qquad \text{(Eqn. 3.4)}$$

where the mesh size, $\xi = bN^{v}$, is the average linear distance between two adjacent crosslinks, with b and N being respectively the Kuhn segment length and the number of Kuhn segments between two neighbouring crosslinks. v is the scaling exponent defined by the polymer solvent interaction.[124]

The effective volume fraction is defined as[125]

$$\phi_{eff} = \frac{Nb^3}{\xi^3} = \left(\frac{b}{\xi}\right)^{\frac{(3v-1)}{v}} \qquad \text{(Eqn. 3.5)}$$

With Equations 3.4 and 3.5, it is visible that shear modulus of these hydrogels in a relaxed state depends on ϕ_{eff} as,

$$G_r = \frac{kT\,\phi_{eff}^{\frac{3v}{(3v-1)}}}{b^3} \qquad \text{(Eqn. 3.6)}$$

It was established that in Figure 3.2A, the observed scaling behavior $G_r \sim \phi^{\sim 2.2}$ indicates a good polymer-solvent interaction with an exponent ~2.25 ($v \sim \frac{3}{5}$)[125]. Thus, we assumed good polymer-solvent interactions ($v = \frac{3}{5}$) [126] in Equation 3.6,

$$G_r = \frac{kT\,\phi_{eff}^{\frac{9}{4}}}{b^3} \qquad \text{(Eqn. 3.7)}$$

Equation 3.7 is the equivalent of the solid line in Figure 3.2A, and it represents the scaling general behavior of the hydrogels.

On the other hand, Figure 3.2B implies that the longitudinal modulus of these hydrogels will follow the inverse law of mixtures.[48,108] This is further probed with the measurement of the longitudinal modulus of the physical networks of polyacrylamide semidilute solutions

(Figure 3.3), meaning that the gel is a "biphasic" medium where the longitudinal modulus of the solid and liquid parts are inversely weighted by their volume fractions (Eqn. 3.3).

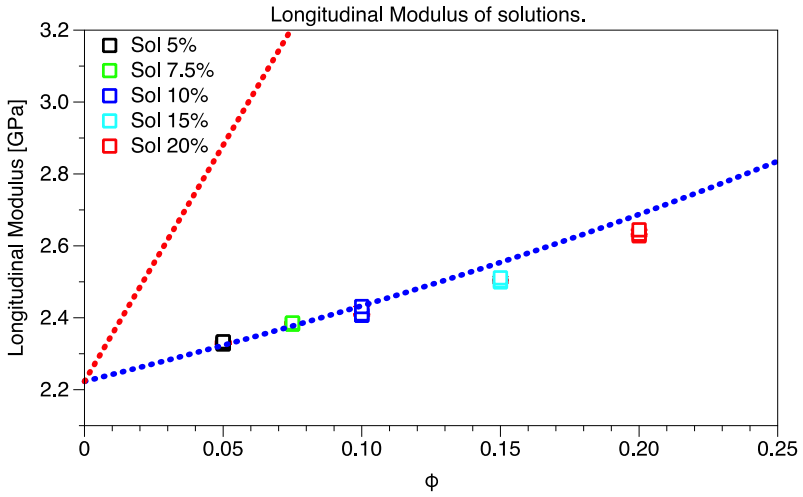

Figure 3. 3 Longitudinal Modulus M vs polymer volume fraction ϕ of polyacrylamide solution mix. This experimental value gives the sets the expected behavior of the gels because the volume fraction is totally controlled only by the amount of polymer added to the mixture. Linear and inverse law of mixtures follow the red and blue pointed line, respectively.

For the polyacrylamide physical network in Figure 3.3, $\phi_{eff}=\phi$ is the unique AA volume fraction where it is observed that it follows the inverse law of mixtures. The linewidth of the Brillouin spectrum also presents a slight increase with the polymer volume fraction as expected, but far from the transition from the liquid to solid phase.[46,47]

The representation of shear modulus in Equation 3.7 involves the Kuhn segment length b as an adjustable parameter. Using b=1.5 nm for good solvency which is the case for these hydrogels, significantly improves the fitting quality of $M_r(\phi_{eff})$ (Figure 3.4). This value of b is typical for flexible polymers like polymethylmethacrylate.[127] Thus, by assuming good polymer-solvent interactions for the hydrogels and the inverse law of mixtures, the scaling of the system

and the Kuhn segment length are justified in a consistent way. Both G_r and M_r can be related to an effective polymer volume fraction, ϕ_{eff}, which is an intrinsic property of the gel that dictates the trends of both moduli.

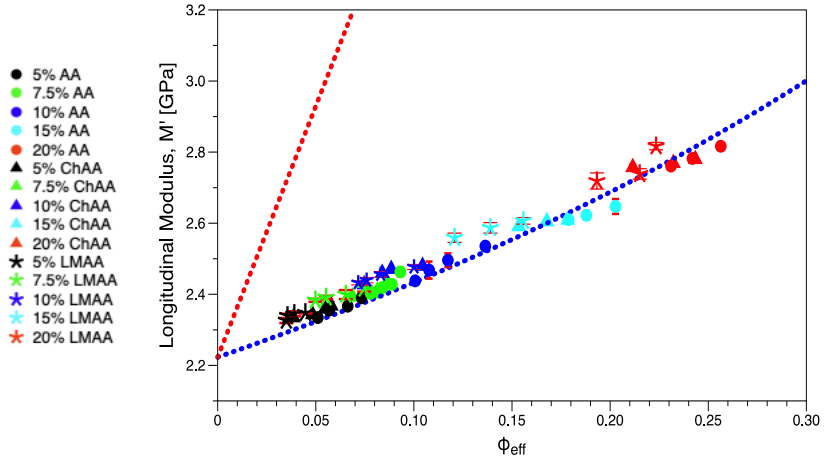

Figure 3. 4 Considering ϕ_{eff} significantly improves the fitting quality of the longitudinal modulus with the inverse rule of mixtures of water (M_w=2.22GPa) and polymer(M_p= 16.35GPa). Blue dotted line is inverse rule of mixtures, red dotted line represents the linear case.

Hence, the correlation between the longitudinal M_r and shear G_r moduli shown in Figure 3.5 is represented (dotted line) by Equation 3.8, derived by combining the description of each moduli in terms of ϕ_{eff}, Equation 3.3 and Equation 3.7.

$$M_r(G_r) = \frac{M_p M_w}{\left(\frac{G_r b^3}{kT}\right)^{\frac{4}{9}} M_w + \left(1 - \left(\frac{G_r b^3}{kT}\right)^{\frac{4}{9}}\right) M_p} \qquad \text{(Eqn. 3.8)}$$

This demonstrates that despite their different physical origins, both shear G_r and longitudinal M_r moduli depend on the effective polymer volume fraction, an underlying intrinsic property of the considered hydrogels. They can be correlated and predicted from each other with the necessary assumptions, namely solvency and Kuhn segment length.

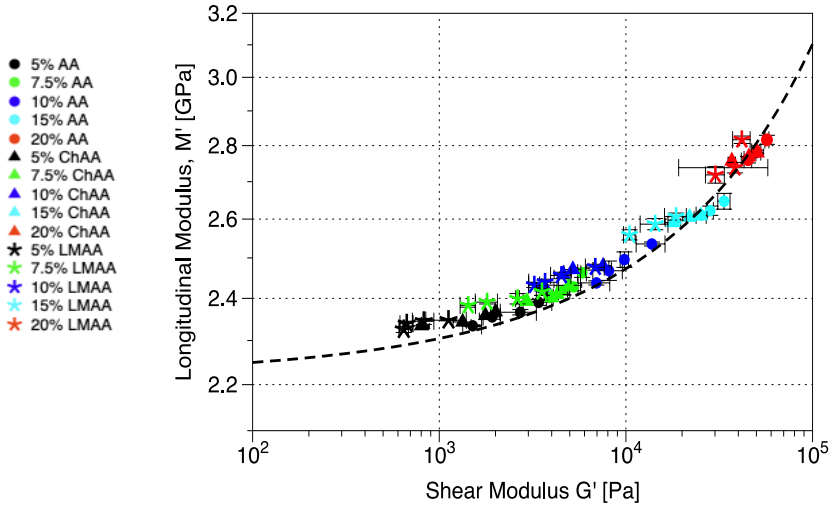

Figure 3. 5 Longitudinal modulus vs shear modulus. Log-log plot of $M_r(G_r)$ of the experimental moduli (symbols) and computed correlation (dashed line, Eqn.3.8) between the two moduli.

3.3.2 Swollen to equilibrium hydrogels.

To obtain swollen-to-equilibrium hydrogels, the hydrogels in the relaxed state were left immersed in DI water for >48 hours, until the weight did not change over time. Afterwards, the *M* and *G* moduli were measured in the same way as the relaxed hydrogels condition. The swelling ratio,[125] Q, was also calculated for each condition of the hydrogels using the weight of the swollen and the relaxed hydrogels, *Weight_*S and *Weight_R*, respectively: $Q = \frac{Weight_S}{Weight_R}$. Some changes in the system were expected, since the hydrogel structure adopts a different force-balance, explained by a different osmotic pressure in the system,[48,125,126] and the swollen polymer network hypothesis links different theories to understand their behavior.[128] Therefore, an impact on the relation $M(G)$ employing the same three different groups of hydrogels is anticipated.

Following the same workflow as for the relaxed state hydrogels, both longitudinal and shear moduli are plotted in Figure 3.6 as a function of a nominal volume fraction

$$\phi_{Sw} = \frac{V_d}{V_s} = \left(1 + \frac{\rho_p}{\rho_s}\left(\frac{W_s}{W_d}\right) - \frac{\rho_p}{\rho_s}\right) \quad \text{(Eqn. 3.9)}$$

where V_d and V_s are the volume of the dry and swollen hydrogels; ρ_p and ρ_s are the density of the polymer and the solvent (water in this case); and W_d and W_s are the mass of the hydrogels in the dry and swollen state. The same color and figure codes are kept except using hollow symbols to distinguish the swollen state from the relaxed state.

Analysing the shear modulus *G,* there is a lack of superposition vs ϕ_{Sw} as seen in Figure 3.6A, including the clear separation of the fits for the different groups suggests that the gels exhibit dramatically different behaviours already in traditional measurements. One behavior cannot be assumed for the three groups of hydrogels, and instead they are clearly separated into groups, each with their own slope obtained from the power law representation: 2.43 for the swollen neutral, 1.22 for the swollen cationic charged condition and 2.44 for the swollen low molecular weight conditions; these groups represented in Figure 3.6A by a solid line, a dotted line and a dashed line, respectively. Due to the different behaviours, it is not possible to assume the same polymer interaction between groups as it was done before with relaxed gels. Similarly, when analysing the Longitudinal Modulus *M,* now a poor inverse rule of mixture law is observed in Figure 3.6B, contrary to the behavior of the relaxed hydrogels (Figure 3.2B). Both the longitudinal and polymer volume fraction seem to be lower, but the apparent dependence is lost. Thus, to understand the distinct behavior of the moduli in the swollen state where the hydrogels reach equilibrium, we proceed with their analysis separately.

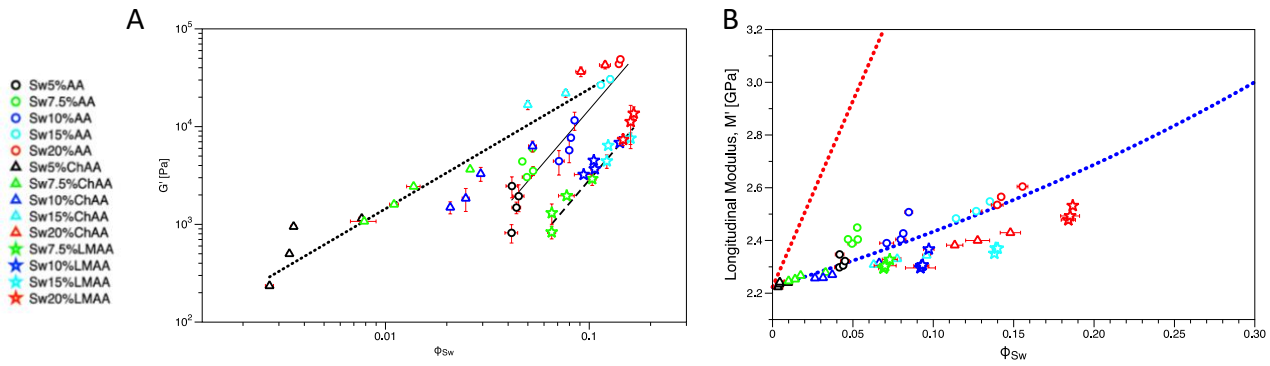

Figure 3. 6 A.Log-log plot of the shear modulus Gs vs ϕ_{Sw} Each condition of the hydrogels shows a distinct behavior. B.Longitudinal modulus M_s vs ϕ_{Sw} of hydrogels swollen to equilibrium exhibiting large scattering of the data points. No trend following the inverse rule of mixtures can be assumed.

Each different condition of hydrogel presented a different swelling ratio, based on the initial polymer and crosslinker concentration. Tables 3.1-3.3 shows the swelling ratio for the different conditions. There is no data for the initial 5% polymer concentration in swollen state because hydrogel lost consistency and it was discarded.

Hydrogel	Polymer initial concentration	Crosslinker ratio [1:polymer=1:x]	Swelling Ratio Q	
Swollen neutral Hydrogels	5%	30	1.24755612	± 0.01899448
		25	1.13535773	± 0.01817962
		20	1.13649038	± 0.02203383
		10	1.00543697	± 0.02394171
	7.5%	30	1.27484779	± 0.0131475
		25	1.24554522	± 0.01440488
		20	1.12936339	± 0.0130814
		10	1.05859909	± 0.01495344
	10%	30	1.2754489	± 0.00840881
		25	1.22708533	± 0.02220582
		20	1.15601009	± 0.0236071
		10	1.06441221	± 0.0234867
	15%	30	1.4592404	± 0.02351288
		25	1.31950147	± 0.03252629
		20	1.2209842	± 0.02139964
	20%	30	1.52042024	± 0.00987445
		25	1.45480364	± 0.01421402
		20	1.31577369	± 0.03925351

Table 3. 1 Swelling Ratios of Swollen Neutral Hydrogels.

Hydrogel	Polymer initial concentration	Crosslinker ratio [1:polymer=1:x]	Swelling Ratio Q	
Swollen cationnic charged Hydrogels	5%	30	17.1322529	± 0.492326769
		25	13.7350325	± 0.314872356
		20	13.2063474	± 0.260568876
		10	6.40385337	± 0.12341006
	7.5%	30	8.2731207	± 0.139733191
		25	6.87267001	± 0.110927692
		20	5.60477027	± 0.34388495
		10	3.27833307	± 0.134946383
	10%	30	5.09483402	± 0.250118857
		25	4.73872909	± 0.377181129
		20	4.06275292	± 0.030779041
		10	2.2863397	± 0.014560859
	15%	30	2.89689159	± 0.046720035
		25	2.5429988	± 0.038070108
		20	2.08924597	± 0.043575288
	20%	30	2.36409719	± 0.029766776
		25	2.12101031	± 0.025614007
		20	1.82679417	± 0.124570869

Table 3. 2 Swelling Ratios of Swollen Cationic Charged Hydrogels.

Hydrogel	Polymer initial concentration	Crosslinker ratio [1:polymer=1:x]	Swelling Ratio Q	
Swollen low molecular weight Hydrogels	7.5%	30	1.348791657	± 0.051446716
		25	1.192771842	± 0.057967338
		20	1.071778612	± 0.027766732
		10	1.023246642	± 0.026581202
	10%	30	1.366600633	± 0.018441865
		25	1.24349826	± 0.028814962
		20	1.095847967	± 0.040910209
		10	1.01770861	± 0.012295901
	15%	30	1.589964078	± 0.028014779
		25	1.553448851	± 0.045012972
		20	1.314134017	± 0.031650077
	20%	30	1.71424115	± 0.055008954
		25	1.590940906	± 0.046326339
		20	1.539956206	± 0.042263875

Table 3. 3 Swelling Ratios of Swollen Low Molecular Weight Hydrogels.

Theoretical frame swollen-to-equilibrium hydrogels.

To estimate the mechanical properties of the hydrogels when they absorb water until they reach equilibrium, it is assumed that the polymer network can swell without any constraint, meaning the network undergoes uniform swelling by the same amount in all directions (i.e., an affine deformation). If this is true, the swelling ratio at the macroscopic level of the hydrogel is equivalent to the deformation $\lambda = Q^{\frac{1}{3}}$ at the microscopic scale of each chain.[129] The Young's Modulus (*E*)

$$\frac{E}{3} = \mu F_{el} \qquad \text{(Eqn. 3.10)}$$

is proportional to the density of the network strands $\mu \sim Q^{-1}$ and the elastic free energy of a network strand

$$F_{el} = \left(\frac{\lambda R_0}{R_s}\right)^2 k_B T \qquad \text{(Eqn. 3.11)}$$

where in the low-swelling regime, R_0 and R_s are the mean-squared end-to-end distance of each chain in the unperturbed state and its fluctuation, respectively.[125,129] Hence, $E \propto Q^{-\frac{1}{3}}$ and since the Young's and shear moduli are proportional to each other for a given Poisson's ratio of the material,[129]

$$G_s \approx G_r Q^{-\frac{1}{3}} \qquad \text{(Eqn. 3.12)}$$

where G_r denotes the shear modulus of the gel in the relaxed state.

This prediction for the shear modulus of swollen hydrogels is plotted vs the experimental data in Figure 3.7. It is observed that the shear modulus of the hydrogels in the relaxed state affected by the swelling ratio ($G_r Q^{-\frac{1}{3}}$) correlate well with the shear moduli G_s in the swollen condition for these hydrogels. Apart of some deviations for the 20%AA samples, the scaling is considered satisfactory within experimental errors and in view of the lack of scalability in Figure 3.6A; a higher Q would be needed to improve the scalability of hydrogels at higher compositions.

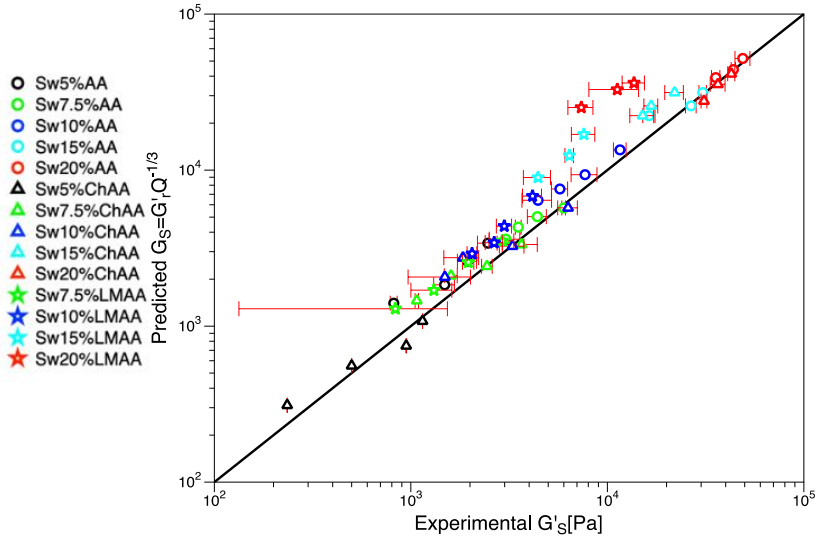

Figure 3. 7 Comparison of the shear modulus measured in relaxed gels G_r affected by the swelling ratio vs the experimental G_S measured on these gels. The black line represents $G_s=G_rQ^{-1/3}$.

Turning to the longitudinal modulus, since it is affected only as a combination of the mixture, meaning the amount of polymer and solvent, the modulus should be represented as the volume-fraction-weighted average of both compositions. Here, the amount of water in the system affects the ϕ_{eff} and allows the introduction of an effective polymer volume fraction for the swollen gels,

$$\phi_{Seff} = \frac{\phi_{eff}}{Q} \qquad \text{(Eqn. 3.13)}$$

Figure 3.8 shows that this ϕ_{Seff} compares well with the experimental polymer volume fraction ϕ_{Sw}.

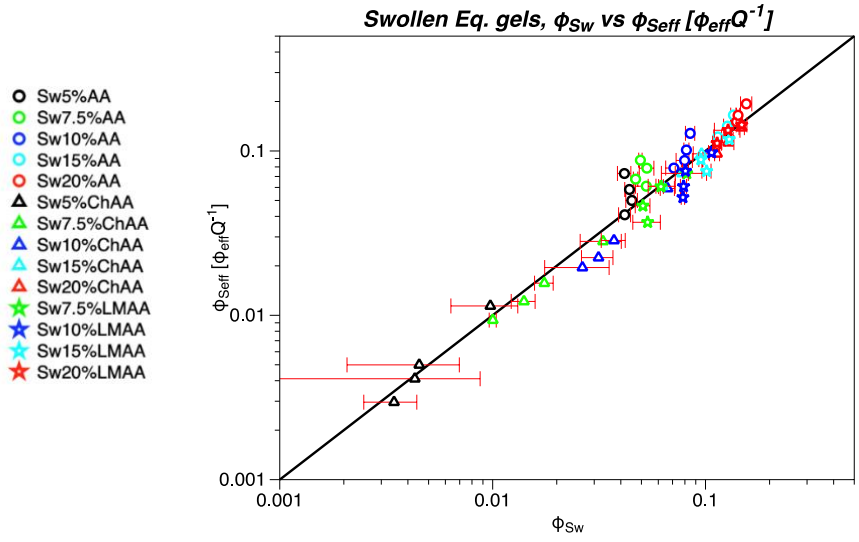

Figure 3. 8 Measured ϕ_{Sw} vs ϕ_{Seff} of Swollen Hydrogels. ϕ_{Sw} represented with Eqn. 3.9 $\phi_{Sw} = \frac{V_d}{V_s}$. While ϕ_{Seff} is calculated with Eqn.3.13, $\phi_{Seff} = \phi_{eff}Q^{-1}$ where ϕ_{eff} refers to the relaxed state and Q is the experimental swelling ratio. Line represents $\phi_{Sw}=\phi_{Seff}$

Figure 3.9 shows that when ϕ_{Seff} is assumed for the M_s of the hydrogels, it also follows the inverse law of mixtures relation (Equation 3.3). Note that the fit without any adjustable parameter is less satisfactory than for the relaxed gels (Figure 3.4) but much better than that using ϕ_{Sw} (Figure 3.6B).

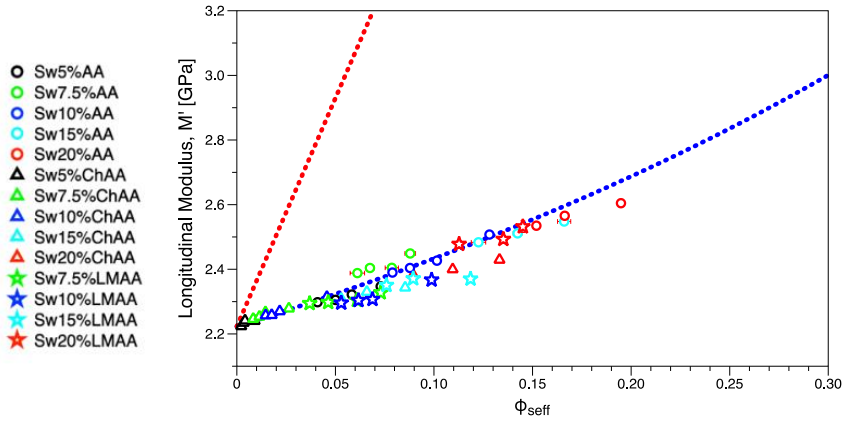

Figure 3. 9 The behavior of M_s seems a better fit following the inverse law of mixtures when considering $\phi_{Seff}(= \phi_{eff} * Q^{-1})$, instead of what is observed in Figure 3.6B.

Thus, both moduli are affected by ϕ_{eff} of the hydrogels prior to swelling, but the longitudinal modulus $M_s(\phi_{Seff})$ depends on the swelling ratio Q, while the shear modulus G depends on the volumetric deformation ($Q^{\frac{1}{3}}$) of the network. Being able to predict these moduli separately, their mutual relationship for the swollen hydrogels can be similar to Equation 3.8 for the relaxed hydrogels, by replacing $\phi_{eff} = \left(\frac{G_r b^3}{kT}\right)^{\frac{4}{9}}$ with

$$\phi_{Seff} = \left(\frac{G_r b^3}{kT}\right)^{\frac{4}{9}} \frac{1}{Q} = \left(\frac{G_S b^3 Q^{1/3}}{kT}\right)^{\frac{4}{9}} Q^{-1} \sim Q^{-0.85} \qquad \text{(Eqn. 3.14)}$$

Unlike Equation 3.8, M_S is not only a function of G_S, but also depends on Q according to Equation 3.14, due to the hydrogel specific swelling, i.e., system dependent ϕ_{Seff} (Q).

$$M_s(G_S, Q) = \frac{M_p M_w}{\left(\frac{G_S b^3}{kT}\right)^{\frac{4}{9}} Q^{-0.85} M_w + \left(1 - \left(\frac{G_S b^3}{kT}\right)^{\frac{4}{9}} Q^{-0.85}\right) M_p} \qquad \text{(Eqn. 3.15)}$$

Based on Equation 3.15, the relationship between M_S and G_S for hydrogels in the swollen state requires additional information of the preceding relaxed state, expressed in their swelling ratio Q. Figure 3.10 displays the experimental $M_s(G_S)$, as well as different lines that the systems

would follow if all the samples had the same Q values (Q=1, 2, 10, 20; represented by different dashed line color). At relaxed state all the samples follow the behavior of Q=1, but since Q changes for the different hydrogels, there is not a single behavior that can be followed for the swollen hydrogels. It is easy to see that the successful superposition obtained in Figure 3.5 for the relaxed gels is not assured for the corresponding swollen state, and as seen before in Figure 3.6A, the hydrogel monomer structure seems to dictate the observed distinct trends of the three systems, as the impact on the extent of swelling (Q) is not unique function of ϕ_{eff}. For example, some of the low molecular weight hydrogels (☆) fall on the upper dashed line computed for Q=1 (which would be the relaxed state), whereas the cationic charged gels (△) conform to higher Q, without the whole group following the same exact trend. For the neutral charged gels (○), $M_S(G_S)$ seems to follow an intermediate Q~1.5. Overall, the estimation of G_S from the experimental M_S data is subject to significant uncertainties due to the inevitable effect of the varying effects of swelling.

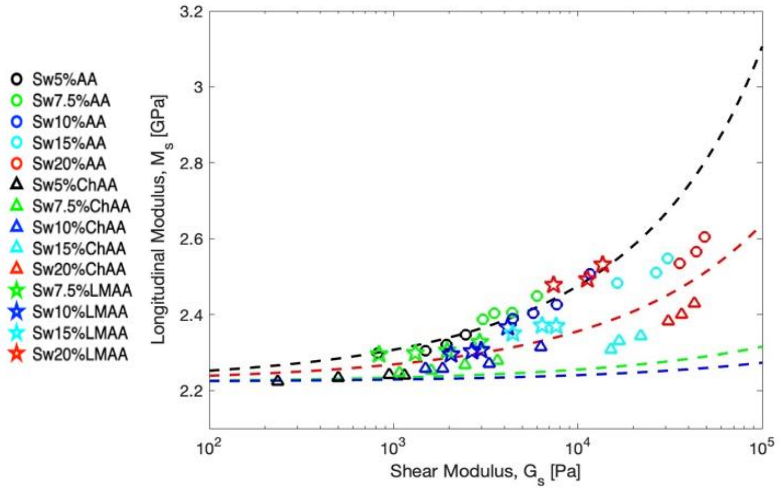

Figure 3. 10 Prediction of the relationship for swollen hydrogels. Log-log plot of experimental M_S vs experimental G_S. Symbols represent the experimental data, while the theoretical prediction of Equation 3.15 assuming a swelling ratio for all the samples is represented with dashed lines [Q=1 (black, for the relaxed state); Q=2 (red); Q=10 (green); Q=20 (blue)]. The experimental data do not follow the same trend because the samples have a different Q.

3.4 Conclusions.

Shear (G) and longitudinal (M) modulus are biomechanical properties of different physical origin, and it is not correct to assume that these quantities are correlated according to a universal relationship. Nevertheless, in many practical settings, different underlying biochemical, physical, and structural changes in the samples are found to affect both moduli in the same manner leading to observed empirical correlations. Previously, the equilibrium swelling theory and Rubber Elasticity Theory have been used to describe and understand the mechanical properties and the swelling-to- equilibrium behavior of hydrogels, considering inherent properties of the hydrogels, such as the polymer-monomer interaction parameter, molecular weight between crosslinks, molecular weight of the monomer, polymer volume fractions in the relaxed and swollen states, and molar and specific volumes of the solvent.[128,130,131] It has also been defined that the charge of the monomers in the system, the pH level, and the presence of salt in the system also affect these swelling properties and hence the mechanical properties of the hydrogel after swelling.[125,131-134] In this Chapter, to describe the global stiffness of a hydrogel, the Rubber Elasticity Theory and scaling concept of semi dilute polymer solutions were employed. This was based on some of the inherent characteristics of the monomer and solvent. An effective polymer volume fraction was calculated to better describe the experimentally measured shear modulus; on the other hand, there is no similar theory to describe the experimentally measured longitudinal modulus.

To understand the mechanical properties of the hydrogels, it is proposed to base them on an effective polymer volume fraction of each hydrogel. It was demonstrated that both the shear G_r and longitudinal moduli M_r of a hydrogel depend on the effective polymer volume fraction, ϕ_{eff}.

Both moduli can be correlated and predicted from each other with necessary assumptions of the hydrogel, namely the solvency and the Kuhn segment length. Although the correlation is still system dependent and not universal, we now provide a physical-explanation of the correlation.

For hydrogels in the swollen state, the force balance changes, and a new explanation of the mechanical properties needs to be considered. Practically, due to the different underlying physics and processes of the different moduli, swelling affects the moduli in the same direction but with different functional forms. Also in this case, a prediction is possible for the mechanical behavior of the hydrogel but each modulus by separate. For the shear modulus, the behavior of the polymer chain at microscopic scale affects the hydrogel at the macroscopic scale of the modulus in a volumetric manner. Alternatively, the longitudinal modulus was affected as an average of the solid and fluid components, and the fit of the effective polymer volume fraction is affected directly by the swelling ratio as Q^{-1}, following the inverse law of mixtures. It is worth noting that in the swollen case, the shear modulus measurements already display a non-universal behavior across different hydrogel formulations, implying that additional information is needed to understand the structure-mechanics relationship in traditional rheology measurements. For the correlation between the two moduli, both are affected by the swelling ratio, determined by the water intake, which also depends on the relaxed polymer volume fraction and the crosslinking density. As a result, a prediction for the moduli of the swollen hydrogels is feasible, provided that information of the relaxed state of the system and the swelling ratio are available. Biological systems are more complex than a controlled hydrogel system, but this work provides fundamental insights as to why empirical correlations have been observed even in such complex systems, i.e. a common dependence of low-frequency shear and high-frequency longitudinal modulus on the different

variables intrinsic to the system; however due to the system-dependent nature of the correlation, an initial calibration curve should be performed for each specific system.

CHAPTER 4: STIFFENING AND DEHYDRATION OF CORNEAL TISSUE AFTER THE CROSSLINKING PROCEDURE*.

4.1 Introduction.

The objective of this chapter is to quantify the stiffening of the corneal tissue after the crosslinking procedure (CXL) via gold-standard mechanical testing methods to estimate how the corneal tissue is affected by subsequent changes in hydration levels (*H*). Previous studies have related in a quantitative model the changes in Brillouin frequency shift to hydration and solid mechanics[15,135] after CXL in samples *ex vivo*. In these, Brillouin shift was measured for a control and a CXL cornea, and the hydration level was changed to obtain a curve of Brillouin shift as a function of hydration. The Brillouin shift changes as a function of hydration consistently in both conditions. It is important to identify and quantify these changes due to hydration and due to solid mechanics, because in the *in vivo* scenario, these might change over time. In a clinical setting hydration level of the cornea can be easily measured by a hydration-thickness relationship. Isolating the effects of CXL is crucial for understanding the physicochemical impact on the tissue, enabling a better characterization of the different CXL procedures and diagnosis of corneal mechanical disorders. Additionally, we studied the depth dependence hydration of the tissue since the tissue is compound of layers with different mechanical properties.

Corneal crosslinking procedure (CXL) is the standard-of-care clinical procedure to treat keratoconus, a progressive corneal disorder resulting in focal thinning and increased focal

* The results on this Chapter have been submitted to the journal IOVS for publication.

curvature with vision loss due to underlying focal corneal weakening. Before corneal crosslinking (CXL), there was no effective treatment to limit the progression of the disease. CXL is the approved clinical procedure to treat this condition, it was introduced in Germany in 2003,[95] and approved in the US as the first FDA approved treatment for keratoconus in 2016.[7] CXL is performed with the objective of increasing the biomechanical strength of the cornea[73,74] to stop keratoconus progression, improving the visual outcome of patients in studies *in vivo.*[13,14,95] This improvement is correlated to a stiffening effect observed in samples *ex vivo.*[73,95] However, there is a dehydration effect also observed with the corneal CXL, and a correlation between mechanical properties and hydration levels in tissue is expected but often overlooked.

The CXL involves the removal of the epithelium layer of the cornea to soak the stromal layer in a solution of 0.1% Riboflavin and 20% Dextran for certain amount of time, followed by UV-A light exposure to induce the photochemical reaction. The riboflavin, used as a photosensitizer that absorbs UV-A light energy to induce covalent bonds between collagen molecules,[8] is generally in a solution including Dextran originally introduced to prevent swelling of the corneal tissue. This is an important step in the procedure because it has been proved that mechanical properties are affected by the hydration of the tissue: an increase in water content leads to a decrease in the overall tissue stiffness.[9-12] Overall, the CXL process results in loss of water content, as observed by the thickness-hydration relationship[12-96] and the thinning of the corneal tissue[13-97] post-procedure. Consequently, there are two separate factors contributing to the observed stiffening of the tissue *ex vivo* following the CXL procedure: the covalent bonds that are created between the collagen-collagen molecules and collagen-proteoglycans by the photochemical reaction with the Riboflavin; and the dehydration experienced by the tissue after

the soaking in the Riboflavin-Dextran solution and the UV-A light exposure. However, the hydration of the tissue *in vivo* is a variable that changes over time. Although there is dehydration after the CXL procedure, this level is recovered after a certain period, returning the corneal tissue hydration to baseline preoperative levels, while maintaining the visual improvement of the patient.[13,14] Therefore, the observed stiffening effect in corneas *ex vivo* should not be presumed to represent the total effect persisting *in vivo* over an extended period after the CXL procedure. This Chapter aims to understand these factors separately and calculate the stiffening effect of only the photochemical crosslinking between molecules, i.e., the effect on the corneal solid tissue network.

Previous studies have investigated the correlation between the biomechanical properties of the cornea and its hydration level, demonstrating that as hydration in the tissue increases, the overall biomechanical strength decreases. These studies include tensile[9-11] and compression test[136] on both regular and crosslinked corneas.[137-139] Additionally, the non-contact method Brillouin Light Spectroscopy (BLS) has been used to further study this relationship, providing more evidence of the hydration-dependent mechanical properties of the cornea in samples *ex vivo*.[15,135,140]

To separate and quantify the contribution of the photochemical effect and the hydration effect on the measurement of the biomechanical properties after the CXL. Porcine corneal buttons were divided into collagen crosslinked and control groups. Afterwards, the hydration level is varied and the Young's Modulus E is measured by compression tests to generate hydration-dependent biomechanical curves of various crosslinking procedures. The tissue is then modeled as a solid

component, a network without pores to accurately determine the real stiffening solely from the photochemical effect.

Hydration of corneal tissue has also been an interesting subject of study for decades beyond CXL procedure. As stated in the *Background* section, the stroma makes 90% of the corneal tissue, it is a layer with parallel sheets of collagen fibrils called lamellae, oriented perpendicular to the surface. Between these lamellae, there is a hydrated proteoglycan matrix with the capacity to absorb water due to its negative charge. In intact corneoscleral tissue, the swelling of the corneal tissue differs between the anterior and the posterior parts of the corneas.[69] This is due to the specific architecture of the anterior part of the stroma, characterized by more disorganized and interweaving collagen fibrils compared to the posterior part of the stroma, with more organized parallel fibrils and lamellae.[67-68] This unique architecture results in a stiffer anterior part of the cornea[71] and resistance to swelling when the corneal tissue is uncorrupted.[69] In this work, the architecture of the corneal buttons after hydration changes were studied with Confocal Reflection Microscopy (CRM), finding a different behavior to the one reported in whole corneoscleral tissue.

4.1.2 Brillouin microscopy used for corneal biomechanics.

Previous work has been done aiming to correlate longitudinal and Young's modulus in the cornea. When accelerated CXL was performed in corneal tissue, and the hydration effect was considered, a ~100MHz increase in Brillouin shift was found. This was equivalent to a ~25% increase in Young's Modulus[5,15] for the corneal tissue based on modulus measured with a home-built compressive stress-strain instrument and reporting the modulus at 15% strain. The Brillouin

dependence of hydration was described accounting for changes in intrinsic corneal properties based on biphasic theory, such as refractive index, density and tissue compressibility.[89,15]

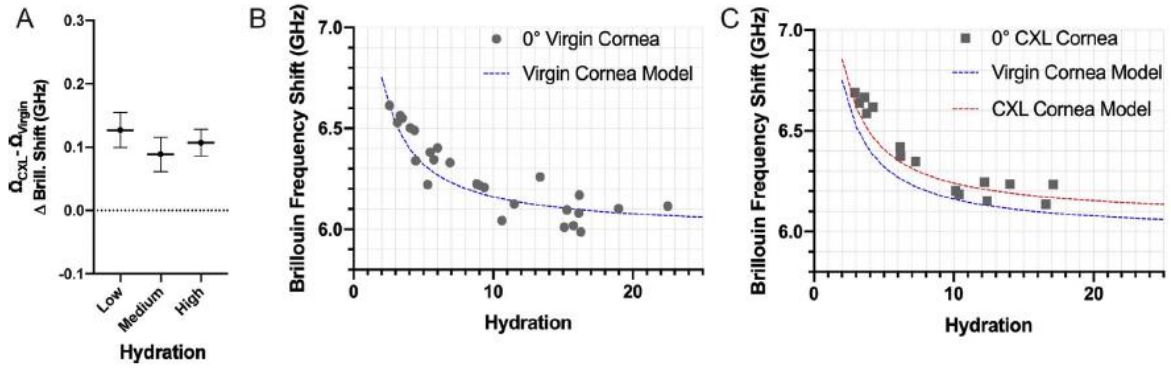

Figure 4. 1 A. Difference in average Brillouin frequency shifts between CXL and virgin corneal buttons varying hydration. B. Brillouin shift of virgin corneas with varying hydration and computational fit. C. Brillouin shift of CXL corneas with varying hydration and computational fit. Adapted from [15].

4.2 Materials and Methods.

4.2.1 Porcine Corneas.

Freshly enucleated porcine eyes were obtained from a slaughterhouse (Wagner Meats, Mount Airy, MD) and maintained in ice until the start of experiments. Eyes were inspected, and damaged or unclear corneas were discarded before starting experiments. For eyes that were selected for experimentation, epithelium tissue was carefully removed with a razor blade, and the cornea was dissected to obtain a 5 mm punched button (Integra Miltex Disposable Biopsy Punch) from the central cornea. Corneal buttons were then randomly assigned to a group for mechanical test: control, accelerated crosslinking (accCXL) and regular crosslinking (CXL).

4.2.2 Corneal Crosslinking.

Riboflavin solution (riboflavin 0.1%, dextran 10%) was prepared and topically applied to the corneal buttons every 3 minutes for 30 minutes. Afterwards, two corneal crosslinking protocols

were applied: the Dresden protocol and an accelerated crosslinking. The Dresden protocol is clinically accepted regular crosslinking (CXL),[95] in which the button is exposed to a constant 365 nm UV-A light (UV Curing LED System, ThorLabs) with a surface irradiance of 3 mW/cm2 (measured with UVS Digital Radiometer) for 30 minutes, applying a drop of riboflavin solution every 5 minutes and an accelerated crosslink protocol,[5,71,141-143] in which the surface irradiance is 9 mW/cm2 for 10 minutes, also applying a drop of riboflavin solution at 5 minutes. In the control group, the buttons were not exposed to UV-A light, but they were immersed in the riboflavin solution for the same amount of time. These are listed in Table 4.1.

Parameter	Group 1	Group 2	Group 3
Protocol	Dresden Crosslinking (CXL)	Accelerated Crosslinking (accCXL)	Control
Soak time (interval) [min]	30 (3)	30 (3)	30 (3)
Treatment time (interval drop) [min]	30 (5)	10 (5)	-
Intensity [mW/cm^2]	3	9	-
Total fluence [J/cm^2]	5.4	5.4	-
Chromophore	0.1% Riboflavin	0.1% Riboflavin	0.1% Riboflavin
Light source	365 nm UV-A light	365 nm UV-A light	365 nm UV-A light

Table 4. 1 Summary of corneal crosslinking protocols.

4.2.3 Corneal Hydration Control.

After crosslinking, hydration level of the cornea (*H*) was controlled by immersing the corneal button in distilled water or left out in air for certain amount of time to induce different levels of hydration or dehydration respectively, similar to other studies.[15,135] Before the mechanical testing, the corneal button was weighed, and afterwards, they were left out to dry in air for at least

72 hours and weighed again. With this information, the hydration level (ratio of the amount of water and the amount of dry mass of the cornea) was measured:

$$H = \frac{(total\ weight\ of\ the\ button - dry\ weight)}{dry\ weight} \qquad \text{(Eqn. 4.1)}$$

4.2.4 Mechanical Testing of Corneal Buttons.

The thickness of the corneal buttons was measured with a digital caliper before the mechanical tests. Dynamic mechanical analyzer (DMA Q800, TA Instruments) was used to perform compression tests. Sandpaper was attached to the top plate of the compression clamp to avoid slippage. The corneal buttons were placed on the bottom plate of the clamp and the top one was brought down to contact, and a 0.001 N force was applied as a preload force to avoid floating of the top plate. A 1N/min compression was applied to the corneal button and stopped at 3N. For the analysis, the points for -1 to -5% compressive strain were taken, and the compressive stress was calculated by dividing the measured force by the area of the corneal button. The Young's Modulus (E) was calculated and reported here for this compressive strain as the tangent of the stress-strain curve.

4.2.5 Theoretical Model to calculate the Modulus of the Corneal Solid Tissue Network.

The corneal tissue was modeled as a hydrated porous material, a biphasic material made up of a solid (α=s) and a fluid (α=f) component. In the case of the corneal tissue, the solid component is the solid tissue network, and the fluid component is the water that hydrates the tissue. Each one of these occupies a volume fraction (ϕ_α) of the mixture, and the mixture saturated ($\phi_s + \phi_f = 1$). The Young's Modulus (E) relates to the shear modulus (G) via the Poisson ratio (v):

$$G = \frac{E}{2(1+v)}, \qquad E = 2G(1+v) \qquad \text{(Eqn. 4.2)}$$

Previous studies have demonstrated that corneal biomechanical properties change as ϕ_f of the mixture changes.[15,135] The variation of the shear modulus can be calculated from the variation of the ϕ_f[144]:

$$G = G_s(1 - \phi_f) \quad \text{(Eqn. 4.3)}$$

where G_s is the shear modulus of the mixture when ϕ_f=0, this is only the solid network of the mixture, without pores and no fluid component, and is the fitting variable to adjust to find the photochemical stiffening effect of the CXL procedure. With Eqn. 4.2 and Eqn. 4.3, *E* can be calculated from G_s and the ϕ_f:

$$E = 2G_s(1 - \phi_f)(1 + v) \quad \text{(Eqn. 4.4)}$$

As the hydration level changes, Poisson's ratio also varies and is calculated in terms of the ϕ_f[145]:

$$v = \frac{H_A - 2G_s(1-\phi_f)}{2(H_A - G_s(1-\phi_f))} \quad \text{(Eqn. 4.5)}$$

Where H_A is the "aggregate" elastic modulus of the solid network[146] and is defined as

$$H_A = \frac{D_0(1-\phi_f)^n}{\alpha(2-\phi_f)^2} \quad *(\phi_f)^{2-n} \quad \text{(Eqn. 4.6)}$$

D_0 is the value of water self-diffusion coefficient ($2.3x10^{-9}\frac{m^2}{s}$ at 25°C);[147] n and α are fit parameters used for hydrated porous materials[148] such as the corneal tissue ($n = 3.236, \alpha = 3.39x10^{-18}\frac{m^2}{Ns}$). Combining Eqn. 4.5 and Eqn. 4.6 with Eqn. 4.4, there is an equation to calculate a theoretical relationship of *E* in terms of the variation of the fluid component ϕ_f i.e. hydration level of the corneal tissue:

$$E = 2G_s(1 - \phi_f) * \left(1 + \frac{\frac{D_0(1-\phi_f)^n}{\alpha(2-\phi_f)^2}(\phi_f)^{2-n} - 2G_s(1-\phi_f)}{2\left(\frac{D_0(1-\phi_f)^n}{\alpha(2-\phi_f)^2}(\phi_f)^{2-n} - G_s(1-\phi_f)\right)}\right) \quad \text{(Eqn. 4.7)}$$

A curve of the Young's Modulus E in terms of hydration level is obtained and fitted with Eqn. 4.7, obtaining the value of Gs, the shear modulus of only the solid tissue network when hydration level is 0. With the correlation between shear and Young's modulus, E_s is calculated as the Young's modulus of only the solid tissue network of each condition: control, accCXL and CXL. The disparity in the E_s observed across the different conditions, represents the real stiffening effect on the biomechanical properties of the corneal tissue, and not a hydration effect.

4.2.6 Confocal Reflection Microscopy.

Cross-sectional images of the corneal tissue were captured using a confocal microscope (Olympus FLUOVIEW 3000) with a 405nm light, and a 20x lens. Corneal buttons were either immersed in water or left out in air for certain amount of time to induce different levels of hydration or dehydration respectively. Afterwards, the button was cut in half, to obtain a cross-section image without the need of further tissue preparation. The ability of the collagen fibrils to reflect light[149] was used to generate high-resolution images without any chemical processing or staining, and only the cutting process required for the cross-sectional imaging. The images were then processed, and the different parts of the cornea (anterior, posterior and total thickness) were measured with the image processing program ImageJ.

4.3 Results and Discussion.

4.3.1 Biomechanical properties of cornea vs Hydration level.

After the CXL, accelerated CXL and control procedure in the samples, hydration level and Young's Modulus are measured. The CXL group, showed a ~4-fold increase of the Young's

Modulus (0.72±0.1 MPa) when compared to the control group (0.17±0.045 MPa). However, dehydration was also evident on the corneal buttons after the CXL procedure, decreasing the hydration level H from 4.07±0.35 in the control condition to 2.06±0.2 after the CXL. This effect is seen in the regular protocol even when the drops of riboflavin to reduce dehydration are periodically applied to the corneal buttons. The accelerated CXL, a protocol to reduce the amount of time of the whole procedure, followed a similar trend, but with reduced effect both in the stiffening of the tissue and the change in hydration level. There was a ~3-fold increase of Young's Modulus (0.53±0.12 MPa) when compared to the control condition, while H decreased to 2.79±0.12 (Figure 4.2).

As stated before, it is known that changes in H will affect E. To further evaluate this correlation, H was modulated after the CXL procedures, immersing the corneal button in water or leaving them out to dry, reaching H levels from 1-12. E was measured afterwards following the same procedure as before, and data points obtained represent the behavior of the Young's modulus vs hydration level obtained for the different conditions. With Eqn.4.7, modeling the corneal tissue as a biphasic material, we fitted the relationship E-H for the different conditions, leaving the Modulus of only the solid tissue network as the fitting variable. The results of the fitting curves for each condition are in Figure 4.3, where every data point represents different samples of each hydration level, increments of 1. The data points of Figure 4.2, i.e. where hydration level is not controlled after the procedure, are represented by a ⋆ symbol.

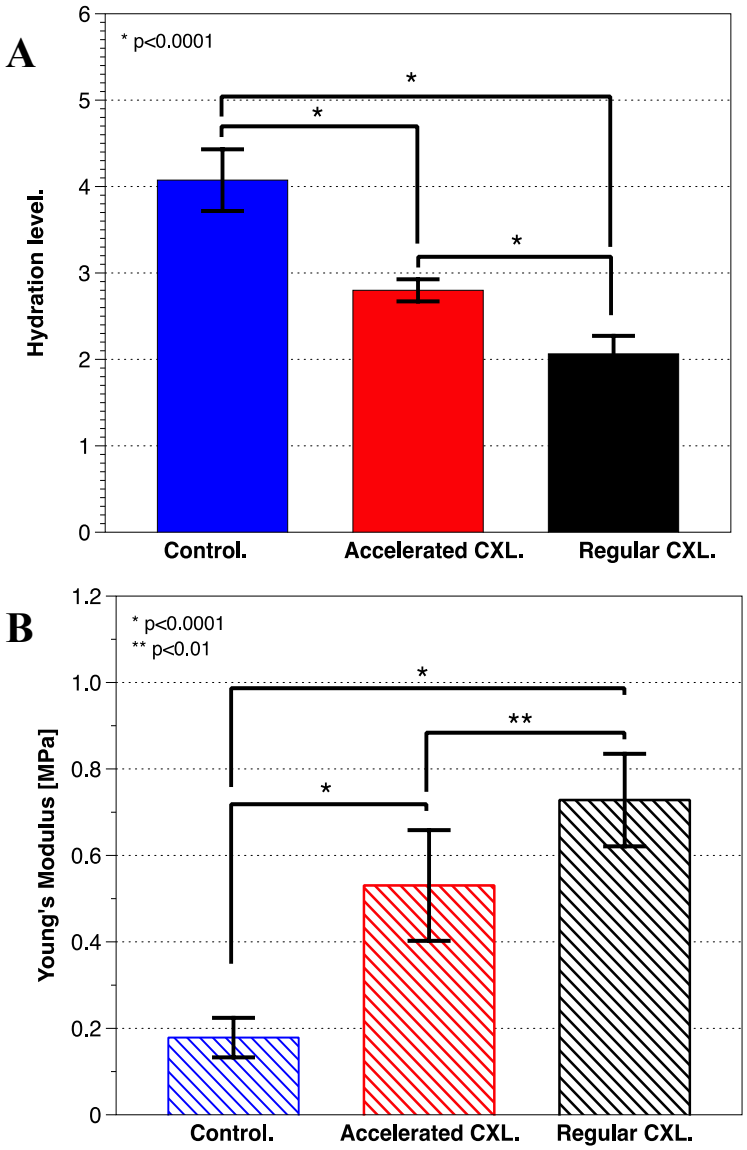

Figure 4. 7 A. Hydration level of the different conditions of the cornea. Hydration level decreases when the CXL procedure is applied. B. Young's Modulus (*E*) of the different conditions of the CXL procedure. *E* increases with both accelerated and regular CXL, but regular CXL shows a higher increase in stiffness.

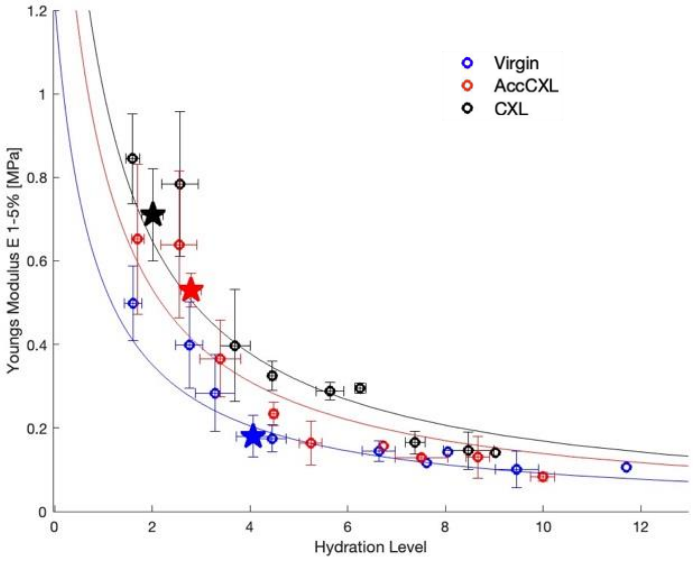

Figure 4. 11 Young's Modulus vs Hydration curves for the different conditions of the CXL procedure. Each point in hydration level represents increments of 1. The ⋆ represents the condition where hydration is the result of the procedure, it is not manipulated after the procedure, same data points as in Figure 4.2.

The fitting variable for Eqn. 4.7 is the shear modulus of the solid network G_s; but E_s is easily calculated with Eqn. 4.2. Since this is a value where the hydration level is 0, with no water in the tissue, the values of the mechanical modulus for this solid network is higher than values of Figure 4.1, where the groups have different levels of hydration. The photochemical stiffening effect due to the crosslinks within the collagen fibrils is calculated (Figure 4.3): there is a ∼1.8-fold increase between the CXL condition (2.25±0.19 MPa) and the control condition (1.22±0.11 MPa); while there is a ∼1.5-fold increase compared to the accelerated CXL (1.85±0.18 MPa). Visualizing these values in Figure 4.2, these would be found where the fitting curves intercept the Y axis, meaning H=0, removing any hydration effect on the Young's modulus of the tissue.

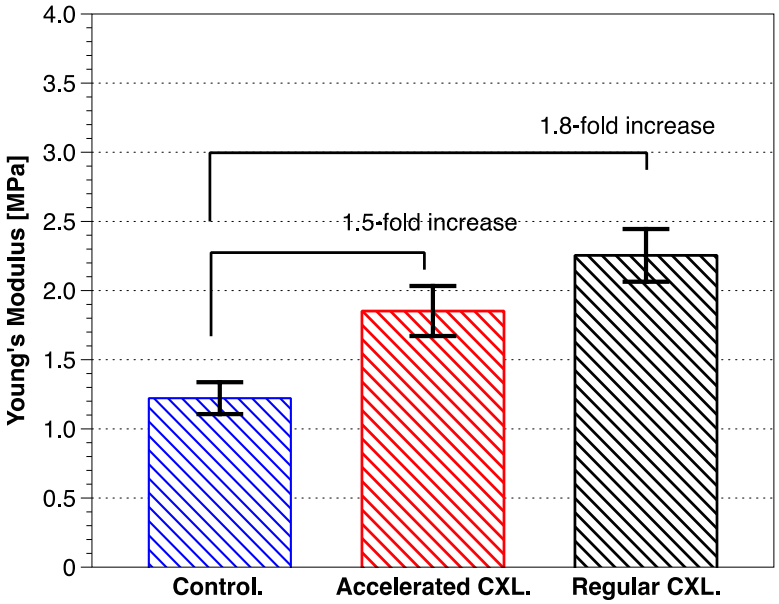

Figure 4. 19. Young's Modulus exclusively attributable to the photochemical effect. The result comes as a fitting parameter of the generated curves of Figure 4.2, modelling the corneal tissue as a hydrated porous material and a biphasic material made up of a solid and a fluid component. Error bars represent a 95% confidence.

This works presents a quantitative model for the biomechanical properties of the cornea, accounting for both mechanical stiffening of the solid tissue network and hydration level of the tissue. Young's Modulus vs hydration level curves were generated for corneal buttons under different conditions (CXL, accCXL and control), including conditions far from the *in vivo* levels. While previous studies have conclude on the importance of the hydration for the biomechanical properties,[9-11,15-140] this model and the resulting modulus-hydration curves (Figure 4.3) allowed to isolate and calculate only the photochemical effect of CXL(Figure 4.4). This model also demonstrates, consistent with previous studies,[137] that the photochemical effect of CXL persists at different hydration levels, with the magnitude of this effect varying depending on hydration. While the photochemical stiffening effect is evident at same hydration levels in the generated curves, the difference is less pronounced in highly hydrated samples compared to those with lower hydration

levels. Whit this model, the fitting variable is the modulus when hydration is zero, not affected by the hydration level, and can be understood as the stiffening of only the solid tissue network of the tissue (Figure 4.4). We theorize that this value can be understood as a more accurate long-term effect of the CXL procedure on the cornea.

Compared to the previous worked that correlated Young's and longitudinal modulus independent of hydration, the 100MHz change in Brillouin was equivalent to a ~25% increase in Young's Modulus[5,15] for Accelerated Crosslinking. However, in this work, we report a ~50% increase of the Young's modulus independent of hydration. The reasons of the discrepancy might be different reasons, for example, the different compression equipment (a home-built equipment and a DMA) and the different compression protocol used for the best results in each case. Additionally, the previous work reported a tangential Young's modulus at 15% strain, while this work presents the tangential Young's modulus at 1-5% strain. Finally, for the previous work and found correlation, while hydration was monitored for the longitudinal modulus measurements, it was not monitored during compression test.

4.3.2 Architecture of the cornea affected by hydration level.

After establishing that hydration is an important variable for mechanical conditions, both in Chapter 3 with hydrogels and part of this Chapter 4, there was an interest to investigate how hydration affects the specific architecture of the cornea: the anterior part of the corneal stroma is highly complex, and visually defined with interweaving fibrils; while the posterior part consists of parallel fibrils. Moreover, The CXL procedure has been shown to affect the cornea with certain a depth dependence. After the CXL, the anterior layer of the cornea within 200 μm has shown a

significant increase in the mechanical properties, while the remaining tissue show minimal effect.[151] This dependence of the chemical crosslinking is important to consider when studying the result of the procedure, and the question that arises is if the hydration of the tissue is also depth-dependent. In corneas *in vivo,* the primary regulator of the tissue hydration is the continuous pumping action of endothelial cells.[152] In contrast, in *ex vivo* corneal samples, hydration is only controlled by the medium in which the cornea is immersed. In this study, the hydration level of the corneal tissue was manipulated to observe its impact on biomechanical properties by immersing the corneal buttons in water, or leaving them to dry out in air. Confocal Reflectance Microscopy (CRM) was used to identify and quantify the thickness changes of the different parts of the cornea.

To analyze how the hydration level affects the tissue in corneal buttons, virgin corneal buttons were immersed in DI water, or left to dry on open air to modulate *H*. The images obtained with CRM were analyzed, the anterior part of the stroma was defined as the section with interweaving fibrils, and the posterior part as the section with parallel ones (Figure 4.5A) and the overall thickness of the corneal tissue was found to linearly correlate to hydration *H*: $Thickness[\mu m] = 368.32 + 188.67 * H$; R^2=0.9064 (Figure 4.5B).

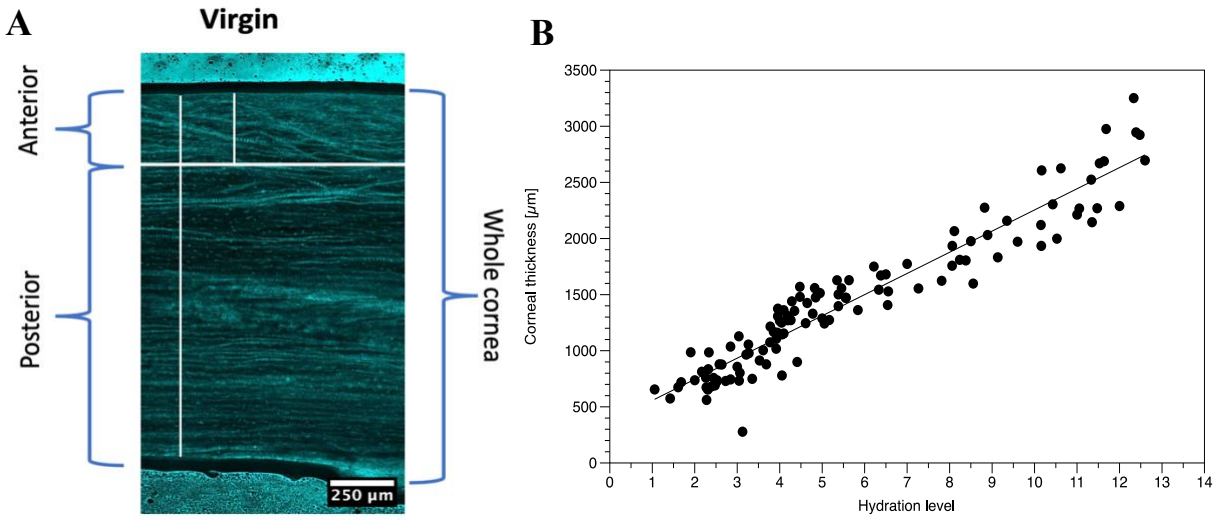

Figure 4. 28 A. Representative image of the corneal tissue with CRM. Anterior part of the stroma is defined as the part with interweaving fibrils. Posterior part is defined as when fibrils are parallel to each other. B. Total thickness, of the cornea at different Hydration levels. Thickness[µm]=368.32+188.67*H; R^2=0.9064.

However, when quantifying the anterior vs posterior parts of the cornea through different hydration levels (Figure 4.6 A), no depth dependence of hydration induced changes in thickness throughout the cornea was observed. The ratio of the anterior/posterior part showed a small increase with hydration level (Figure 4.6 B), showing that at some point at highly hydrated conditions, the anterior part swelled more in percentage than the posterior part. This change of the architecture of the cornea at high hydration levels is important and a new result.

As mentioned in the *Background* and introduction of this Chapter, the specific architecture of the cornea gives the tissue a mechanical depth-dependence. The anterior third of the stroma presents a significant increase of stiffness that helps on the maintenance of corneal curvature.[69] Additionally, the anterior part of the cornea also exhibits strong resistance to swelling when immersed in water, while the posterior part of the cornea absorbs water and swells,[69] as

demonstrated by electron microscopy on fixed corneoscleral tissue immersed in water for different days (Figure 4.7).

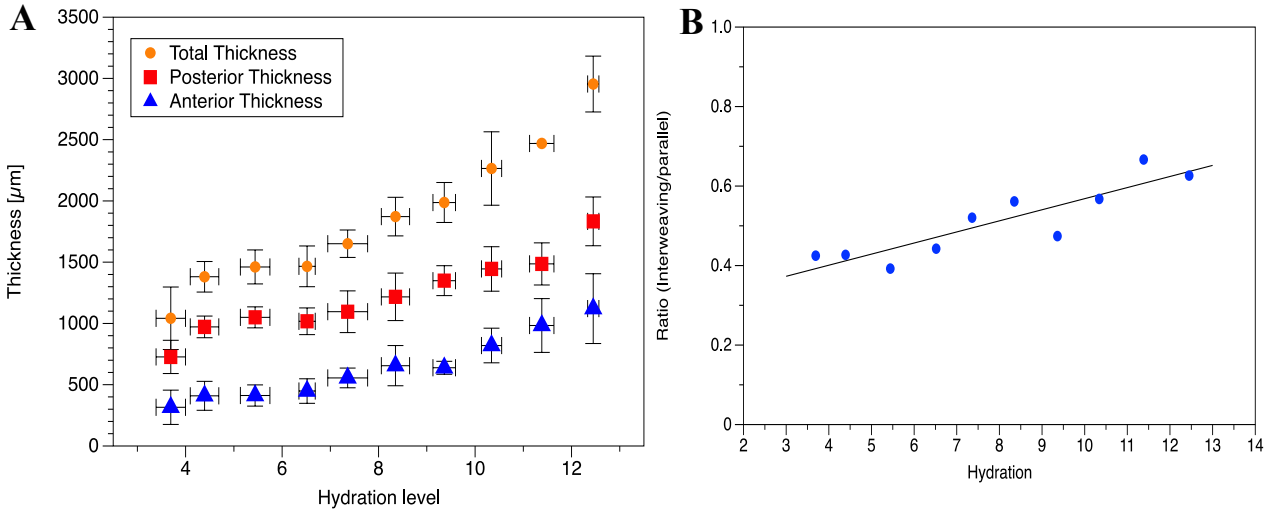

Figure 4. 41 A. Anterior and posterior sections of the cornea at different hydration levels. Al low hydration levels H<3, the sections definition is not clear. B. In the corneal buttons, the anterior/posterior ratio of the cornea increases at high hydration levels. Linear regression

$y = 0.0279x + 0.2892$; $R^2 = 0.7909$; p-value < 0.001

Confocal Reflectance Microscopy CRM allows to generate high-resolution images without any chemical processing or staining due to the ability of the collagen fibrils to reflect light.[149] In accordance with a previous study,[69] when using corneoscleral tissue, the anterior part of the cornea presents resistance to swelling, while the rest of the cornea swells significantly. Furthermore, the difference of conditions with or without the epithelium was studied, in order to investigate if this layer presents extra resistance to swelling, not finding any real difference between these Epi-on, Epi-off conditions (Figure 4.8).

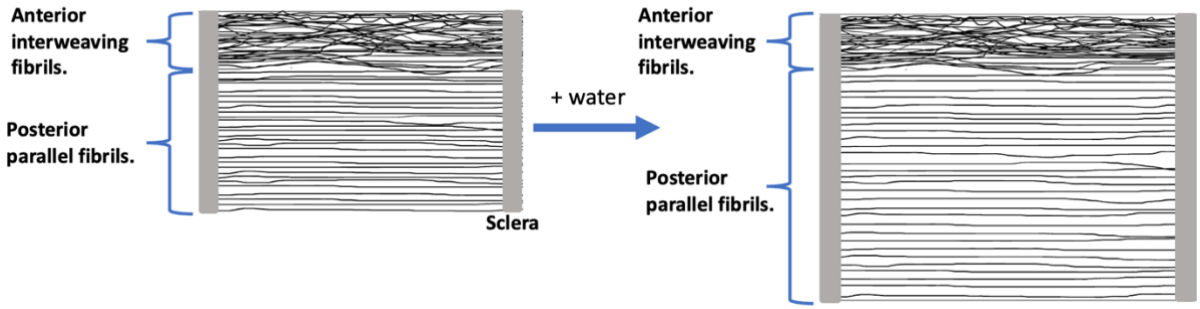

Figure 4. 54. In corneoscleral tissue, the anterior part of the cornea resist swelling when the hydration level of the tissue increases.

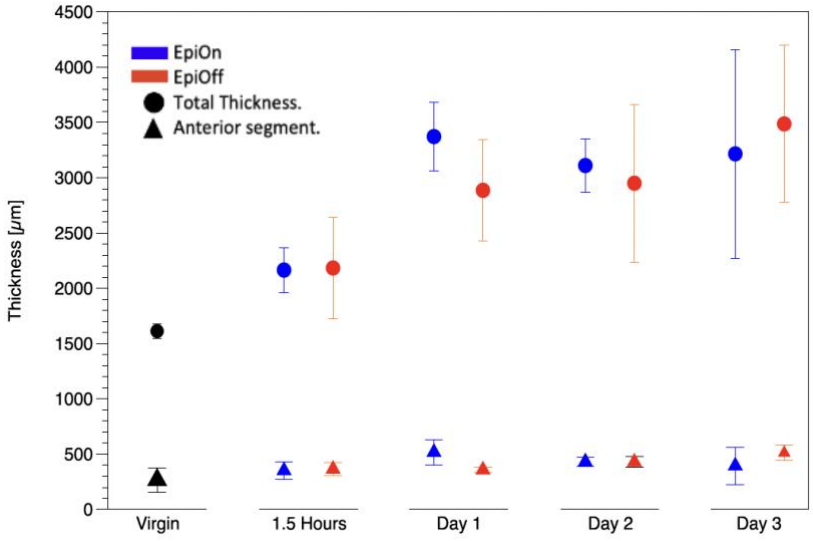

Figure 4. 45. Hydration of corneoscleral tissue. Whole corneas with a scleral ring present thickening of the whole tissue, but a low increase of thickness in the anterior segment of the stroma, where the tissue is more complex compared to the posterior segment, where collagen fibrils and lamellae are parallel to each other. These results match the ones found by Müller, Pels & Vrensen [69].

However, the object of study in this work was the corneal tissue presented as corneal buttons, so the architecture of the cornea under hydration was studied in this condition. The corneal buttons were immersed in water or left out in air to dry for different time within 3 hours. The result was that at highly hydrated conditions (>6), the anterior part of the cornea also presents swelling as seen in Figure 4.6A, and even increasing the ratio of interweaving/parallel lamellae, meaning

that the anterior part with interweaving lamellae presents greater swelling than the posterior part at some point (Figure 4.6 B). Representative images of these cases are in Figure 4.9.

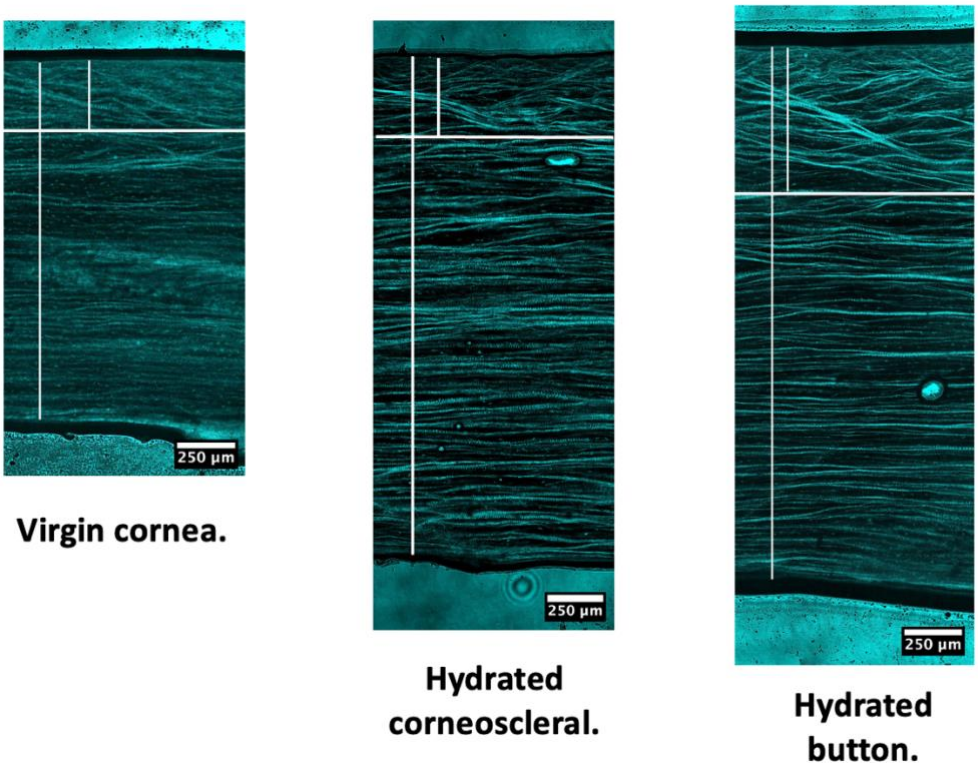

Figure 4. 63. Comparison of a virgin corneal tissue, a hydrated corneoscleral tissue and a hydrated corneal button. The anterior stroma characterized by interweaving lamellae presents resistance to swelling in the corneoscleral tissue, while in the button it seems become thicker together with the posterior.

The difference between the corneoscleral tissue and the corneal button is the ease of water penetration into the tissue of the latest. In the corneal button, the stroma is exposed to the water on the sides of the button, while in the corneoscleral tissue, the sclera presents a barrier of the water penetrating the tissue (Figure 4.10). We theorize that this is why corneal buttons achieve comparable high levels of hydration, calculated by corneal thickness, within hours compared to days in corneoscleral tissue.

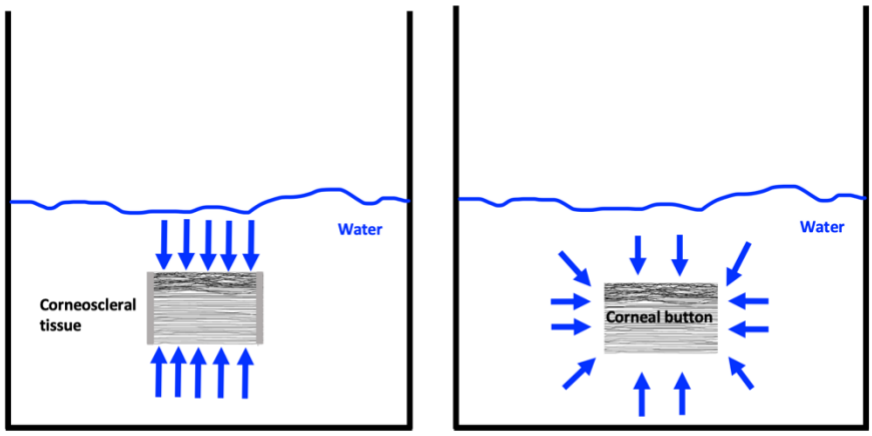

Figure 4. 70. Illustration of the ease of water penetration into the corneal tissue. The scleral tissue represents a natural barrier for hydration of the stroma. Corneal buttons achieve comparable high levels of hydration, calculated by corneal thickness, within hours compared to days in corneoscleral tissue.

4.4 Conclusion.

This works presents a quantitative model to calculate the stiffening effect of the CXL procedure, by separating the photochemical crosslinking of the solid tissue network, and the tissue dehydration. Not considering tissue dehydration when measuring the effects of the different CXL procedures may lead to an overestimation of the stiffening effect. By calculating only the stiffening due to the photochemical crosslinking, we aim to better estimate how the corneal tissue is affected *in vivo,* where hydration level changes after the CXL, eventually reaching a basal steady state. Given that hydration of the tissue is an important characteristic of the mechanical properties of the cornea, we studied how hydration affects the tissue. Our results suggest that the hydration of corneal buttons is different to hydration of corneoscleral buttons, possibly due to different boundary conditions in water transport. This is an important behavior to consider when designing *ex vivo* experiments that involve highly hydrated conditions.

CHAPTER 5: EVALUATING BRILLOUIN SPRECTORSCOPY VS YOUNG'S MODULUS IN THE NONLINEAR REGIME OF THE CORNEAL TISSUE.

5.1 Introduction.

As defined in the *Background* section, the cornea has a specific architecture that provides unique characteristics for the transparency, stiffness, and appropriate curvature for acute vision. The stroma is ~90% of the corneal thickness and its made up of collagen fibrils arranged in lamellae that run parallel to the corneal surface. This means that the cornea is an anisotropic tissue, with a different configuration in the radial direction and the tangential direction of the tissue.

This anisotropy also affects the biomechanical properties of the cornea. As most soft biological tissues, the cornea has a typical non-linear stress-strain relationship,[12,74] and it is important to define the type of modulus and the level of strain or stress in which calculations or experiments are done in the nonlinear mechanical curve. As explained with Figure 2. 5 Typical nonlinear stress-strain curve for a soft tissue. The Young's modulus is the slope of the of the curve at a specific stress/strain., there are different regions for this nonlinear curve: a linear region at low strains called toe region; followed by a region where there is an evident change of modulus with strain, known as the heel region; and finally a more linear relationship at higher strains, which is maintained until failure.[60] Also, as explained in the *Background*, the collagen molecule organization dictates this nonlinear behavior: in the tangential direction there will be a higher modulus than in the radial direction, due to the directionality and the different events when the collagen molecule is being stretched.

Furthermore, the corneal tissue is under constant multidirectional stress and strain, due to intraocular and extraocular forces. Intraocular pressure (IOP) is one of these constant forces (Figure 5.1) with minimal variation according to activities during the day.[80]

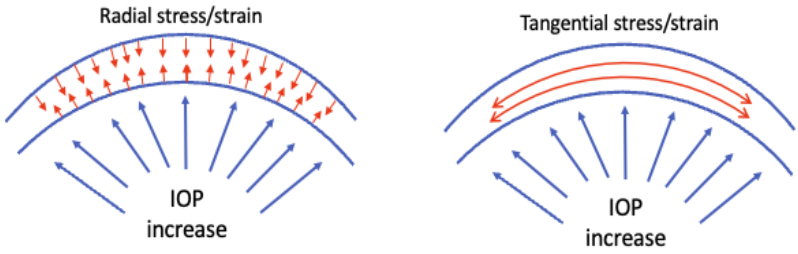

Figure 5. 1 Multidirectional stress/strain on the cornea due to IOP variation.

These changes in the IOP are reflected in the general stiffness of the cornea due to its nonlinear mechanical behavior, and this effect has been proved before with load-displacement indentation methods,[82] optical elastography techniques[17-20] and simulations.[19,83] However, Brillouin technology has failed to measure the nonlinearity of the cornea, showing no changes on the corneal tissue modulus when IOP increases.[20] This is generated large controversy in the field putting into question the mechanical interpretation of Brillouin signatures. This chapter aims to resolve this controversy.

Our hypothesis is that Brillouin is sensitive to material mechanic nonlinearity, but its observed behavior is due to the anisotropy of corneal mechanical properties and in the geometry of the IOP-induced stress compared to the geometry of the mechanical measurements. Indeed, in material science and optical fiber sensors for other engineering applications, Brillouin technology

is often considered gold-strandard for strain sensing exactly based on material mechanic nonlinearity (Figure 5.2).[153-155]

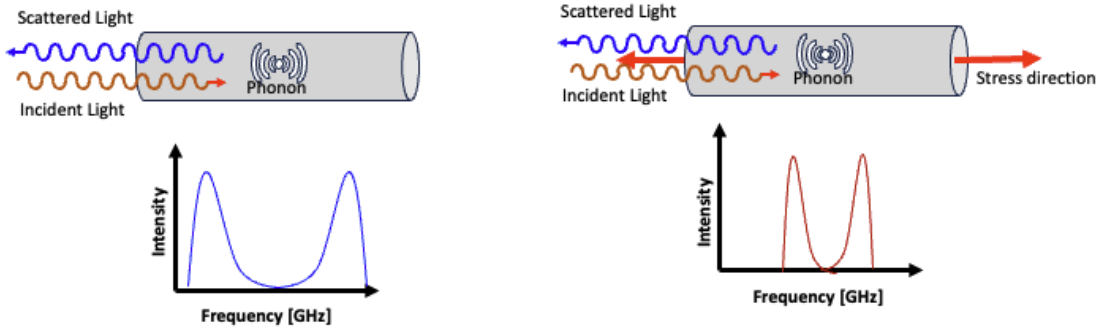

Figure 5. 2 Brillouin technology is gold-standard for strain/stress sensing in optical fibers and material science. When load is applied in the parallel direction of the Brillouin measurement, there is a difference in the Brillouin spectrum, meaning that the mechanical properties of the material is changing.

Interestingly, in this application, Brillouin also has shown to be insensitive to transverse a transverse load (Figure 5.3),[156,157] because Brillouin measurements are purely uniaxial.

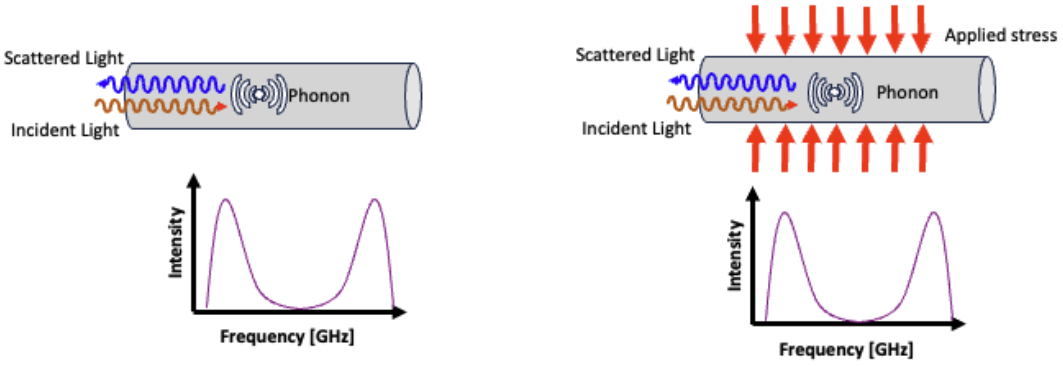

Figure 5. 3 Brillouin technology is insensitive to transverse load. Due to the uniaxial nature of Brillouin spectroscopy, and the longitudinal modulus, Brillouin has been proved to be insensitive to a transverse load on fiber optics.c

We hypothesize an analogous situation is occurring in the cornea, where so far Brillouin measurements have only been performed in the radial direction, i.e. perpendicular to the main direction of the IOP-induced stress. In this Chapter, the uniaxial longitudinal modulus is measured for the cornea at different IOP levels, and two directions radial vs tangential direction. Furthermore, for validation and mechanistic understanding, the mechanical nonlinearity of the cornea at different directions is studied by using a Dynamic Mechanical Analysis (DMA) for compression and tensile tests within the ranges of stress/strain that the cornea is exposed to when IOP changes. This will allow us to study the differences of nonlinearity of the cornea at different directions of the tissue.

5.2 Materials and Methods.

5.2.1 Intraocular pressure in porcine corneas.

Freshly enucleated porcine eyes were obtained from a slaughterhouse (Wagner Meats, Mount Airy, MD) and maintained in ice until the start of experiments. Eyes were inspected, and damaged or unclear corneas were discarded before starting experiments. For eyes that were selected for experimentation, epithelium tissue was carefully removed with a razor blade, and the cornea with scleral tissue was dissected and placed in a Barron Artificial Anterior Chamber (BAAC, Barron Precision Instruments), design to support and maintain an adequate pressure of donor corneal tissue in transplants. This instrument allows us to manipulate the pressure force on the cornea by pumping phosphate-buffered saline (PBS) solution into the BAAC. Intraocular pressure levels of 10, 20 and 30 mmHg were chosen for these experiment, levels that are not far from the normal levels of IOP (10-21 mmHg), or levels of ocular hypertension (>21 mmHg).[158,159]

5.2.2 Brillouin Light Spectroscopy (BLS).

The Barron artificial chamber with the corneas was mounted on an inclinational stage, allowing for free 360º movement. For these experiments, the modulus at the radial direction, perpendicular to the surface pf the cornea, was measured at 0º with respect of the laser, while the tangential modulus was measured at 60º due to physical constrains of the set up (Figure 5.4). Another control that was performed for this experiment was to maintain the cornea at the same IOP level of 10 mmHg, while doing the same measurement in the same time frame as if the IOP was changing. This will discard any dehydration effect that could be the reason for the stiffening of the tissue.

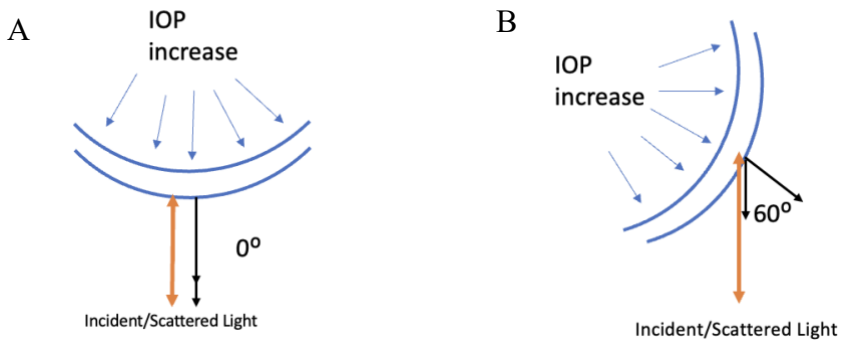

Figure 5. 4 A. Measuring longitudinal modulus in the radial direction. B. Measuring longitudinal modulus in the most tangential direction possible.

The Brillouin microscopy set up described in the *CHAPTER* 2: BACKGROUND section was used to measure the frequency shift. For these experiments, a 660 nm continuous wave laser (Torus, Laser Quantum) with a power ~30mW was focused onto the sample by an objective lens (20X/0.4NA, Olympus), with a transverse resolution of ~1 µm and an axial resolution of ~5.7 µm. Step size of the image is 20 µm per pixel in the X-direction, but almost no movement in the Y direction, to always scan the same portion of the cornea. Image acquisition (EMCCD Andor Camera) with an exposure time of 30 ms.

To measure the changes in mechanical properties with IOP, we start with an IOP level of 10 mmHg, and after 15 consecutive scans the IOP is rapidly increased to 20 mmHg. After other 15 consecutive scans, the IOP is again rapidly increased to 30 mmHg. This means that the whole experiment is 45 linear scans, and it takes ~3.5 minutes. To avoid fluctuations due to the rapid change of IOP, the last 10 of every 15 scans were chosen as representative. In both radial and tangential directions, the scan is long enough to include the entire corneal tissue. At the end, the Brillouin shift reported is an average of the whole tissue of 10 scans per IOP.

Given the natural variability between corneal values and their modulus, the differences of the longitudinal modulus at 20 and 30 mmHg IOP is presented as % compared to the value of the 10mmHg IOP.

5.2.3 Measuring thickness of the cornea.

Corneal thickness is accurately measured with a pachymeter. Pachymeters uses ultrasound to measure the corneal thickness. In this case, the probe was placed on the central part of the cornea and by varying the IOP, the radial strain was measured. A curve of radial strain dependent on IOP can be obtained, which was then used to for the stress-strain curves at the radial and tangential directions.

5.2.4 Compression test for radial stress-strain mechanical curve.

To recreate the stress-strain curve of the nonlinear mechanical behavior of the radial direction of the cornea, the strain at the different values of 10, 20 and 30 mmHg IOP were used.

5- mm corneal buttons (Integra Miltex Disposable Biopsy Punch) from the central cornea were used. With DMA (Q800, TA Instruments) and 8mm plates a strain-controlled compression of the cornea was performed at a strain ramp of -2%/min to -10%. Knowing the radial strain equivalent to 10, 20 and 30 mmHg IOP from the pachymeter readings, the Young's modulus of these values ±1 was calculated as the slope of this stress-strain curve.

5.2.5 Tensile test for tangential stress-strain mechanical curve.

To recreate the stress-strain curve of the nonlinear mechanical behavior of the radial direction of the cornea, also the strain at the different values of 10, 20 and 30 mmHg IOP were used. In this case, the tangential tensile stress of the cornea created by the IOP was estimated using the Young-Laplace equation:[160,161]

$$\sigma = \frac{R*IOP}{2d} \qquad \text{(Eqn. 5.1)}$$

Where σ is the tangential stress, IOP is the intraocular pressure, *R* is the mean radius of the cornea (8.45mm)[162] and *d* is the corneal thickness measured by pachymetry at specific IOP.

After calculating the stress equivalent to the different IOP levels, a stress controlled tensile with a ramp stress 0.005 MPa/min to 0.025 MPa test was performed in corneal strips, and the Young's modulus of the specific stress values was calculated as the slope of this stress/strain curve.

5.3 Results and Discussion.

5.3.1 Brillouin shift changes varying IOP levels.

Representative images of the results of the Brillouin shift at the radial direction are in Figure 5.4 A. The whole cornea is scanned and an average the Brillouin shift, represented as a heat map, is reported as the Brillouin shift of the tissue. The values of 20 and 30 mmHg IOP have an increase <0.1% with respect to the 10 mmHg IOP (Figure 5.5 B).

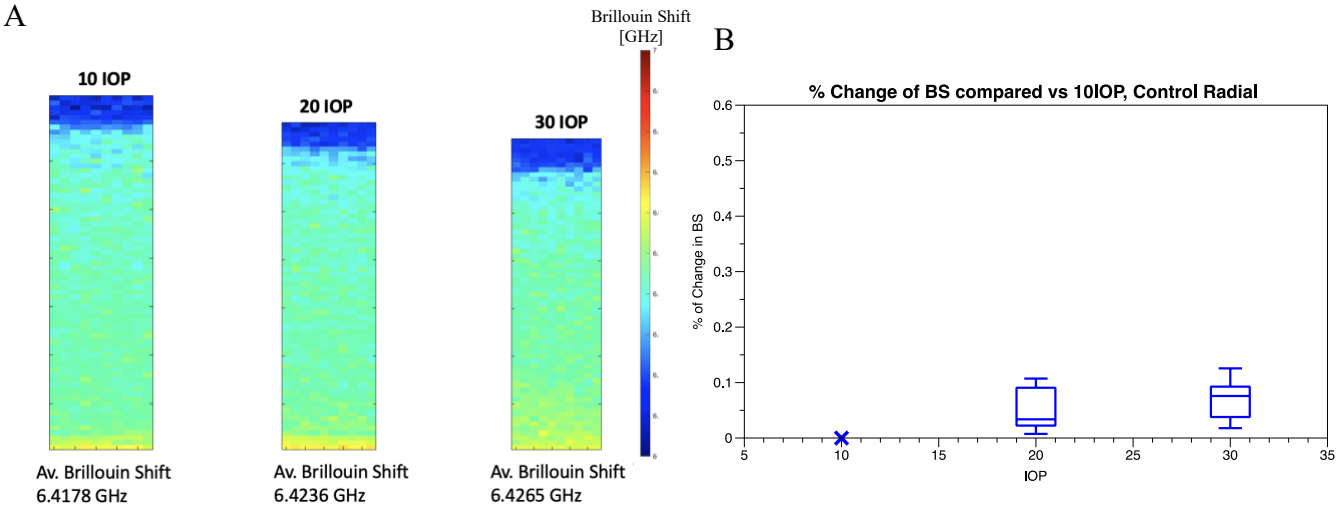

Figure 5. 5 A. Representative images of the Brillouin shift scan of 10, 20 and 30 mmHg IOP values at the radial direction. B. Percentage change of the Brillouin shift with the different IOP values.

Brillouin shift at the tangential direction is presented in Figure 5.6. Now the Brillouin shift of the 20 and 30 mmHg IOP conditions represent an average of ~0.19% and ~0.33% respectively (Figure 5.6B).

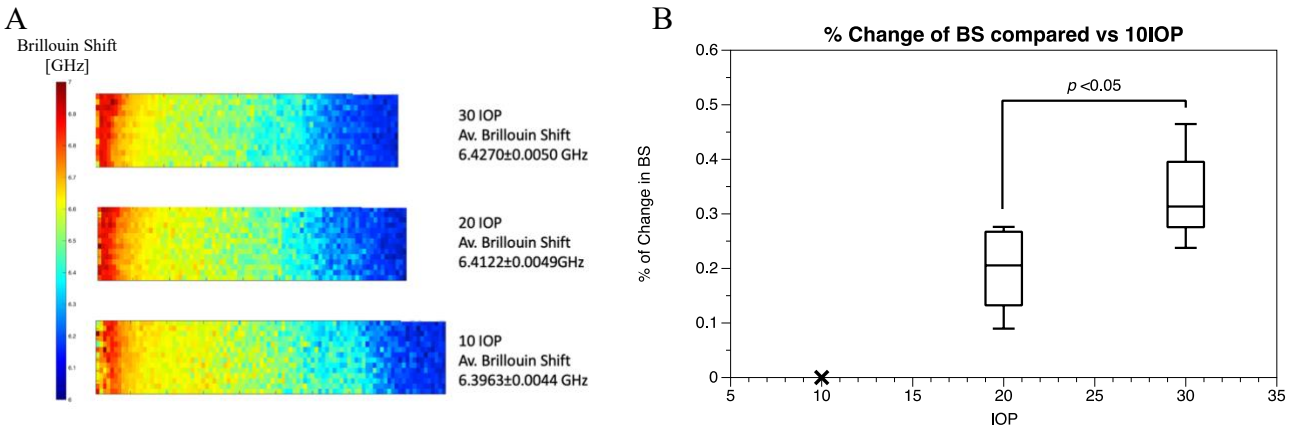

Figure 5. 6 A. Representative images of the Brillouin shift scan of 10, 20 and 30 mmHg IOP values at the tangential direction. B. Percentage change of the Brillouin shift with the different IOP values.

The time and dehydration control of the corneas was performed at the same direction of the tangential direction (as in Figure 5.4B). For this control, the cornea was maintained at 10 mmHg IOP, and the same scan was performed, thus, in the same time frame as the previous experiment. To compare to the experiment where IOP is changing, the different scan lines grouped with the same colors in Figure 5.6A will be the same scan lines as in Figure 5.7, as representative images of this control. In this case, the % change of the Brillouin shift of the different groups is also <0.1% (Figure 5.7 B).

All these results can be visualized together in Figure 5.8. These experiments suggest that when the anisotropy of the cornea, as well as the nature of Brillouin spectroscopy are considered, Brillouin can see the nonlinearity of the tangential direction.

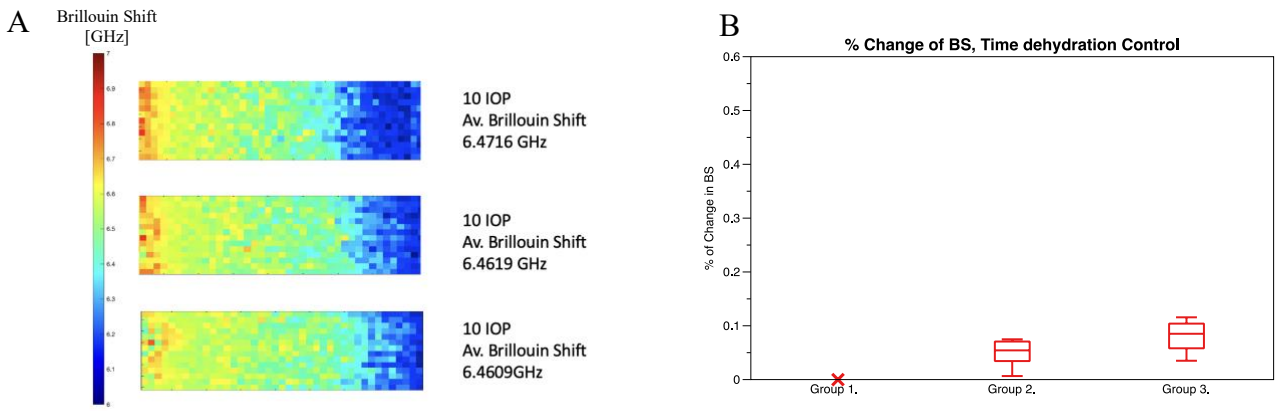

Figure 5. 7 A. Representative images of the Brillouin shift scan of 10 mmHg IOP at different time frames equivalent to the experiment where IOP changes. B. Percentage change of the Brillouin shift with the different IOP values.

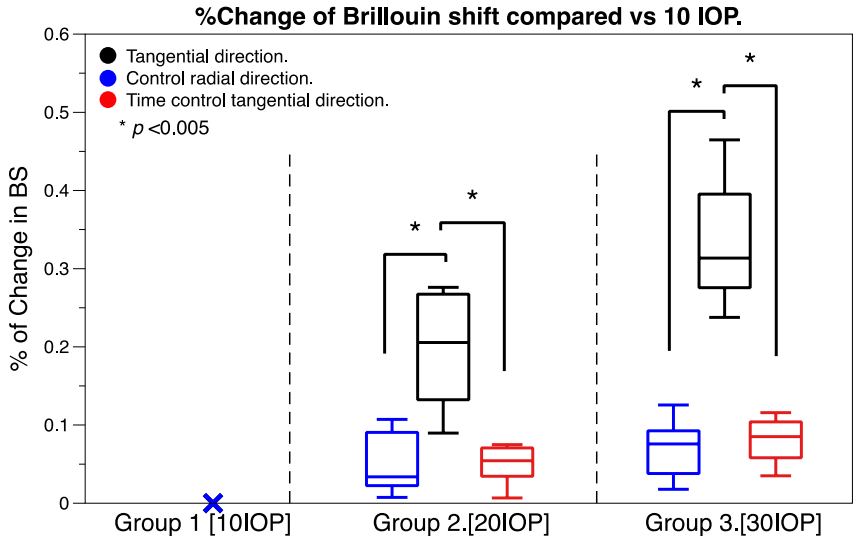

Figure 5. 8 Compilation and comparison of experiments of Brillouin shift at tangential and radial directions. Control of radial direction and control of time/dehydration have a significantly lower % change when compared to the IOP-changing tangential Brillouin shift.

5.3.2 Analysis of depth-dependence change of the modulus.

An interesting effect that can be seen in the IOP changing Brillouin shift, is the depth dependence of the cornea. It has been established before that the anterior part of the cornea presents stiffer mechanical properties, and it is of interest to analyze if this configuration changes when IOP changes. To analyze if there is any depth-dependence of the change of Brillouin shift with changes of IOP, the cornea was divided into three equal sections (anterior, central and posterior). It was observed that, when comparing 10 to 20 and 30 mmHg IOP, while the central and posterior parts of the cornea seem to present a small increase, the anterior part presents a significantly bigger effect (Figure 5.9). This means that the most anterior part of the cornea is the one that is suffering the most stress when the IOP is changing.

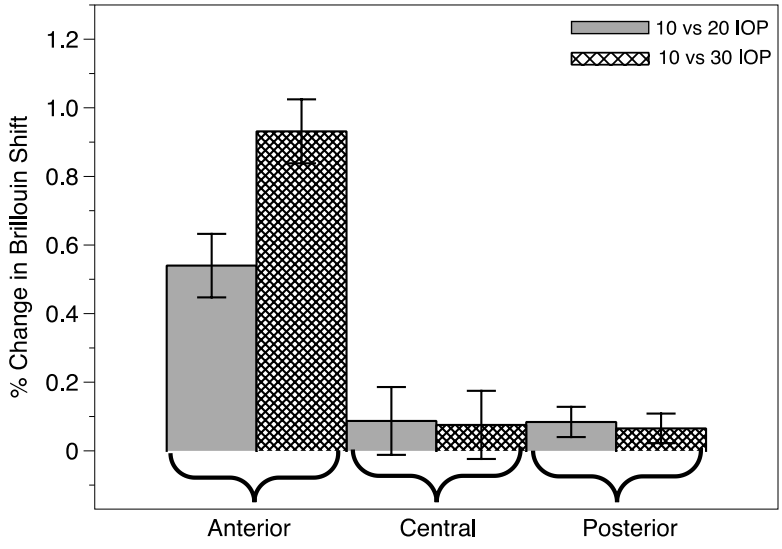

Figure 5. 9 Brillouin shift % changes of different parts of the cornea at the tangential direction. The anterior part of the cornea seems to have the biggest effect when the Brillouin shift changes. While central and posterior part experience a smaller effect.

When doing the same analysis for the radial direction, it was also observed that the anterior part experiences a bigger change in Brillouin shift when compared to the central and posterior

parts. However, the effect is still lower than the one observed at the tangential direction (Figure 5.10).

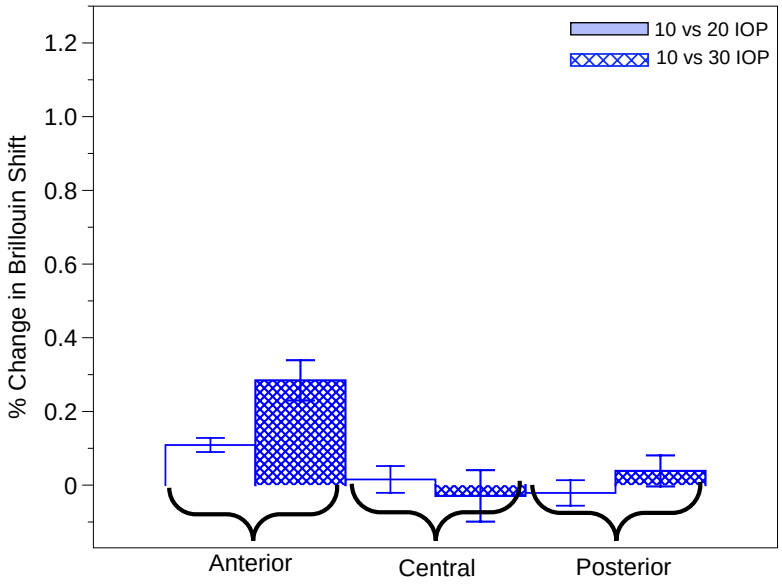

Figure 5. 10 Brillouin shift % changes of different parts of the cornea at the radial direction. Posterior of the cornea still exhibit a higher effect than central and posterior part, but the effect is lower than at the tangential direction.

5.3.3 Compression and tensile test of the cornea equivalent to different IOP levels.

To investigate the reason of why Brillouin sensitive to the tangential nonlinearity but not to the radial direction, we now recreated the stress-strain curves of the tissue at the different directions. Due to the anisotropy of the cornea and the specific layout of the collagen fibrils and lamellae, the radial stress is a lot lower than the tangential stress.[163] By first measuring the radial strain along the different IOP levels, the stress-strain curves are recreated for the different directions of the cornea. The corneal thickness was measured with an ultrasonic pachymeter for different IOP levels, allowing to calculate the radial strain that is presented in Table 5.1 and in Figure 5.10, with a strain <5%.

IOP	Radial strain	SD
2	0	0
5	-0.0102693	0.0068689
10	-0.0165072	0.00888492
15	-0.0247734	0.0109377
20	-0.0321387	0.0112055
25	-0.0424235	0.00961364
30	-0.0461731	0.00945885
35	-0.048205	0.01009825
0	-0.0077674	0.00505806

Table 5. 1. Radial strain at different IOP levels.

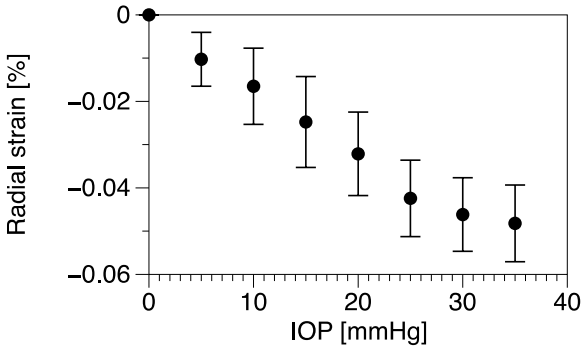

Figure 5. 11 Radial strain at different IOP levels.

With these values, first the radial stress-strain curve was recreated with a compression test performed with DMA on corneal buttons from the central part of the cornea. Then the Young's modulus was calculated as the slope of the curve at the point where the strain ± 0.01 is equivalent to the IOP. This is the modulus at a strain of -0.0165± 0.01 to represent 10 mmHg IOP ; -0.0321± 0.01 to represent 20 mmHg IOP; and -0.0461 ± 0.01 for 30 mmHg IOP (Figure 5.11). The ratio of modulus compared to the condition of 10 mmHg IOP is calculated and the results are presented in Table 5.2.

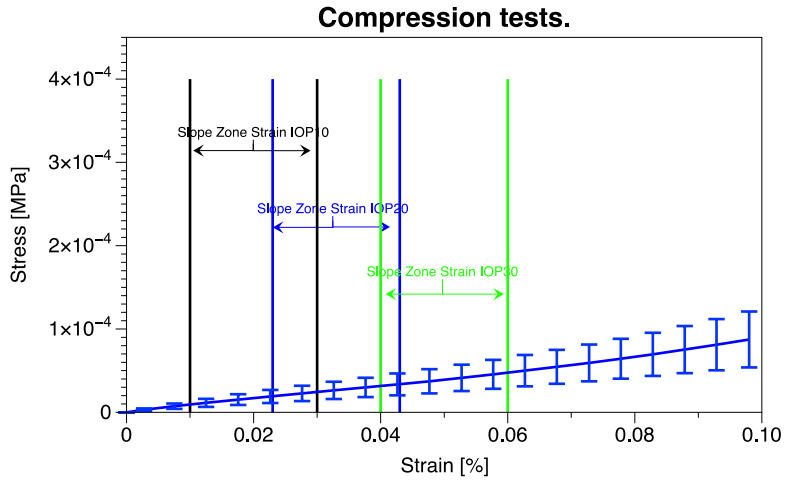

Figure 5. 12 Stress-strain curve at the radial direction of the cornea. The curve seems to be in the initial linear part of the typical J-curve, the toe region.

Strain %	IOP [mmHg]	*E* [KPa] ± SE	Ratio change *E* vs 10 IOP
0.0165±0.01	10	0.756 ± 0.013	-
0.0321±0.01	20	0.745 ± 0.030	0.986
0.0461±0.01	30	0.769 ± 0.029	1.017

Table 5. 2 Characteristics of the stress-strain curve at the radial direction.

Then to recreate the stress-strain curve at the tangential direction, the Young-Laplace equation (Eqn. 5.1) is used to estimate the tangential stress of the cornea at different IOP levels. This equation yields in the tangential stress of the cornea given the IOP, the corneal thickness previously measured with the ultrasonic pachymeter, and the average radius of the cornea. For this test, corneal strips were cut from fresh corneas, and placed on the DMA for tensile test, the Young's modulus is calculated as the slope of the curve at the specific point where the tangential stress is

calculated. These specific points are color coded in Figure 5.12 and in Table 5.3, along with the ratio of change of the Young's modulus on the equivalent IOP points.

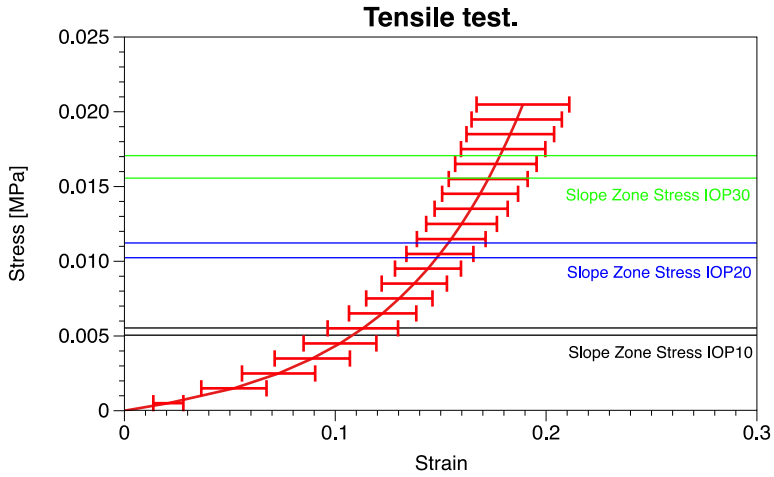

Figure 5. 13 Stress-strain curve at the tangential direction of the cornea. Curve obtained with tensile stress of a corneal strip. The curve shows more the typical *J-curve* shape, different from the linearity at the radial direction.

Stress [Kpa]	IOP [mmHg]	*E* [MPa] ± SE	Ratio *E* vs 10 IOP	Strain (with 10 IOP) %
5.29 ± 0.2434	10	0.101 ± 0.02	-	-
10.73± 0.495	20	0.197 ± 0.058	195	3.93 ± 1.08%
16.313 ±0.753	30	0.303 ± 0.082	299	6.4 ± 1.89%

Table 5. 3 Characteristics of the stress-strain curve at the longitudinal direction.

The change of the modulus at the radial and tangential direction is plotted in Figure 5.13. These results suggest that the cornea has a very different nonlinear behavior in the radial and the tangential directions. The difference is evident to the point that the stress and strain that changes in IOP produce is in the toe region for the radial direction, meaning there is no change of the modulus. Conversely, in the tangential direction, the stress/strain values lie in the heel region,

where there is an evident change of the modulus from one point to another. These results behave are comparable to those found with Brillouin spectroscopy and are presented in Figure 5.7.

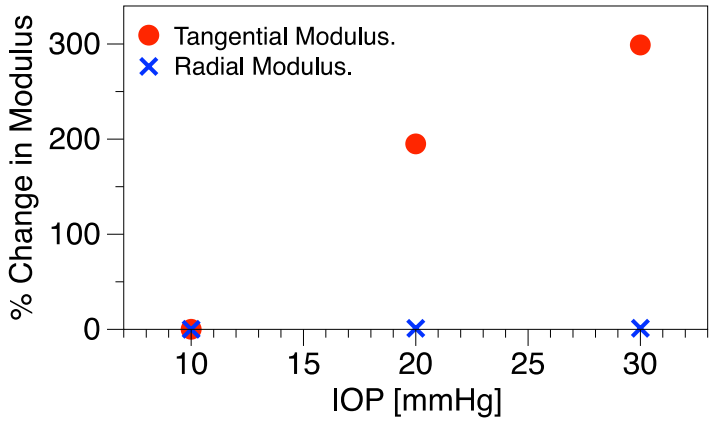

Figure 5. 14 Changes of the Young's modulus at the radial and tangential direction.

5.4 Conclusion.

On this chapter we demonstrated that the nonlinearity of the corneal tissue can be measured with Brillouin technology, and perceived controversy is easily resolved when the anisotropy of the cornea and the physics of Brillouin technology are considered. Brillouin spectroscopy is a uniaxial measurement of the longitudinal modulus, where a transverse load will not affect the measurements; but it is Gold-standard for strain/stress sensing for load parallel to the reading. Furthermore, the corneal tissue has collagen fibrils/lamellae that are parallel to the surface and it was demonstrated with the Young's modulus that the stress-strain nonlinear curves in the radial and tangential differ from each other, changing significantly the modulus in the tangential direction, but maintaining the same mechanical properties in the radial direction, all of this in the 10 to 30 mmHg IOP changing regime.

In this work we provided evidence with the Brillouin shift that the anterior part of the cornea might be suffering a bigger change than the central and posterior parts. This could be due to a combination of the mechanical nature of the cornea, with stiffer mechanical properties on the anterior part, and by being the most outer part of the cornea that would suffer the most strain when the IOP increases.

Future directions for this work could include the study of how hydration affects the nonlinearity of the cornea at the different directions. On Chapter 3, free swelling of an isotropic sample allowed us to predict how the different moduli are changing. However, this is not the case of the anisotropic tissue of the cornea, that only changes in the radial direction when the hydration level changes. But compression and tensile tests have shown that hydration also affect the mechanical modulus in both directions, as it was observed in Chapter 4 for radial direction, and previous works for tangential direction.[139] To further understand the mechanical properties of the cornea, the next step is to compare and quantify how hydration is affecting the different moduli in the different directions. Moreover, Brillouin microscopy can also be considered to study the mechanical changes of the cornea divided in different sections (anterior, central, posterior); including the change of architecture of the cornea observed in Chapter 4 at highly hydrated conditions.

CHAPTER 6: CONCLUSIONS AND SCIENTIFIC CONTRIBUTIONS.

This work investigated and provided a better understanding of the Brillouin measured longitudinal modulus (*M*) and its validation when it is compared to Gold-standard shear (G) or Young's modulus (*E*).

Chapter 3 resulted in a fundamental and truly physical understanding of a previously empirical correlation between *M* and *G*. This was done on hydrogels that can be considered controlled samples, where *G* was explained by theoretical models and a theory could be assumed for *M*. However, it was also understood that as the system gets more complicated, and more variables enter the equation to define the modulus, the correlation of the moduli also becomes complicated because they rely on different physics. This work also investigates an important topic of discussion in Brillouin spectroscopy, which is the insensitivity to highly hydrated samples (>90% water). At this regime, the water dominates the Brillouin measurements, and the correlation appears to be lost. However, at hydration levels closer to physiological levels, the correlation is clear. This work was presented at the international conference of the International Society for Optics and Photonics (SPIE) in 2023. And it was published in the Journal Biomacromolecules, an ACS Publication.

Chapter 4 provides a quantitively study of the effects of the crosslinking procedure (CXL), important to treat ectatic disorders. The CXL efficiency *in vivo* is attributed to *ex vivo* measurements of stiffening the tissue, however for this there are two different effects: the photochemical crosslinking of collagen molecules, and dehydration of the tissue. The cornea hydration level changes with time, a physiological effect that is not usually considered on these *ex*

vivo measurements. Previous work have reported the decoupling Brillouin shift dependence on hydration and solid mechanics after CXL procedure by analyzing how hydration level affect corneal physiological properties. The analogous work is needed with a gold-standard procedure, which in this case is compression test by DMA. By taking into account the dehydration of the tissue and treating the cornea s a biphasic tissue, we were able to use theoretical models to decouple how the different events affect the mechanical properties of the cornea. The result is that we quantified the stiffening of the tissue due to only the photochemical crosslinking of the solid part of the corneal network, which we believe it could be a value similar to the real effect *in vivo.* Furthermore, we studied how the hydration affects the architecture of the cornea, finding that treatment of the sample can affect the architecture, suggesting a new variable to consider when planning experiments. This work was presented at the international conference of the Association for Research in Vision and Ophthalmology (ARVO) in 2023.

Finally, Chapter 5 studies a discrepancy of Brillouin technology, the lack of ability to capture the nonlinearity of the corneal tissue. We demonstrated that Brillouin spectroscopy can measure the mechanical nonlinearity of the cornea when the physical and mechanical anisotropy of the cornea and the unidirectionality of the longitudinal modulus are considered. Additionally, we studied the nonlinearity accordingly to the anisotropy of the cornea, this is in the radial and tangential directions. This work also opened an interesting point of investigation with Brillouin spectroscopy, which is to investigate if there is any mechanical nonlinear depth dependence of the cornea. This because of an analysis in which the anterior part of the cornea seems to suffer the biggest mechanical modulus change. This work was presented at the international conference of the Association for Research in Vision and Ophthalmology (ARVO) in 2024.

REFERENCES

1. Scarcelli, G., P. Kim, and S. H. Yun. In vivo measurement of age-related stiffening in the crystalline lens by Brillouin optical microscopy. Biophys. J. 2011;101:1539–1545.
2. Scarcelli, G., W. J. Polacheck, H. T. Nia, K. Patel, A. J. Grodzinsky, R. D. Kamm, and S. H. Yun. Noncontact three-dimensional mapping of intracellular hydro-mechanical properties by Brillouin microscopy. Nat. Methods. 2015;12, 1132–1134.
3. Conrad, C., et al. Mechanical Characterization of 3D Ovarian Cancer Nodules Using Brillouin Confocal Microscopy. Cellular and Molecular Bioengineering. 2019;12, 3, 215-226.
4. Carlo Bevilacqua, Héctor Sánchez-Iranzo, Dmitry Richter, Alba Diz-Muñoz, and Robert Prevedel, Imaging mechanical properties of sub-micron ECM in live zebrafish using Brillouin microscopy. Biomed. Opt. Express. 2019;10, 1420-1431.
5. Webb JN, Su JP, Scarcelli G. Mechanical outcome of accelerated corneal collagen cross-linking evaluated by Brillouin microscopy. J Cataract Refract Surg. 2017;43(11), 1458-1463.
6. Rad, M. A.; Mahmodi, H.; Filipe, E. C.; Cox, T. R.; Kabakova, I.; Tipper, J. L. Micromechanical Characterization of 3D Bioprinted neural cell models using Brillouin Microscopy. Bioprinting 2022, 25, e00179
7. Belin MW, Lim L, Rajpal RK, Hafezi F, Gomes JAP, Cochener B. Corneal cross-linking: current USA status report form the cornea society. Cornea 37(10), 1218-1225 (2018).
8. Randleman JB, Khandelwal SS, Hafezi F. Corneal cross-linking. Surv Ophthalmol 2015; 60:509–523.
9. Hatami-Marbini H, Rahimi A. Effects of bathing solution on tensile properties of the cornea. Experimental Eye Research 2014; 120:103-108.
10. Hatami-Marbini H. Hydration dependent viscoelastic tensile behavior of cornea. Ann Biomed Eng. 2014;42:1740–1748.
11. Hatami-Marbini H, Rahimi A. The relation between hydration and mechanical behavior of bovine cornea in tension. J Mech Behav Biomed Mater. 2014;36:90–97.
12. Hatami-Marbini H, Etebu E, Rahimi A. Swelling Pressure and Hydration Behavior of Porcine Corneal Stroma. Current Eye Research 2013; 38(11):1124-1132.
13. Mazzotta C, et al. Long term results of accelerated 9 mW corneal crosslinking foe early progressive keratoconus: the Siena Eye-Cross Study 2. Eye and Vision 2021; 8:16.
14. Caporossi A, Mazzotta C, Baiocchi S, Caporossi, T. Long-term results of riboflavin ultraviolet a corneal collagen cross-linking for keratoconus in Italy: The Siena Eye Cross Study. Am J Ophthalmol 2010;149:585–593.
15. Webb JN, Zhang H, Roy AS, Randleman JB, Scarcelli G. Detecting mechanical anisotropy of the cornea using Brillouin microscopy. Trans Vis Sci Tech. 2020;0(0):2367.
16. Roberts C, Dupps Jr WJ, Crawford Downs J. Biomechanics of the eye. Kugler Publications. Amsterdam, The Netherlands, 2018.

17. Ambroziński, et al. Acoustic micro-tapping for non-contact 4D imaging of tissue elasticity. Sci. 2016;Rep. 6.
18. Zvietcovich F, Larin KV. Wave-based optical coherence elastography: The 10-year perspective. Prog Biomed Eng (Bristol). 2022;4(1):012007.
19. MG. Sun, T Son, J Crutison, V Guaiquil, S Lin, L Nammari, D Klatt, X Yao, MI Rosenblatt & TJ Royston. Optical coherence elastography for assessing the influence of intraocular pressure on elastic wave dispersion in the cornea, Journal of the Mechanical Behavior of Biomedical Materials. 2022;128.
20. Nair A, Ambekar YS, Zevallos-Delgado C, Mekonnen T, Sun M, Zvietcovich F, Singh M, Aglyamov S, Koch M, Scarcelli G, Espana EM, Larin KV. Multiple Optical Elastography Techniques Reveal the Regulation of Corneal Stiffness by Collagen XII. Invest Ophthalmol Vis Sci. 2022;63(12):24.
21. Nguyen TM, Aubry JF, Fink M, Bercoff J & Tanter M. In Vivo Evidence of Porcine Cornea Anisotropy Using Supersonic Shear Wave Imaging. Invest. Ophthalmol. Vis. Sci. 2014;55(11):7545-7552.
22. Caponi, S., Passeri, A., Capponi, G. et al. Non-contact elastography methods in mechanobiology: a point of view. Eur Biophys J. 2022;51, 99–104.
23. B. Schroyen, D. Vlassopoulos, P. Van Puyvelde & J. Vermant. Bulk rheometry at high frequencies: a review of experimental approaches. Rheol Acta. 2020;59:1-22.
24. Still T, Oudich M, Auerhammer GK, Vlassopoulos D, Djafari-Rouhani B, Fytas G & Sheng P. Soft silicone rubber in phononic structures: Correct elastic moduli. Phys Rev B. 2013;88, 9: 094-102.
25. Landau LD, Lifshitz EM. Theory of Elasticity, vol. 7. Course of Theoretical Physics. (2nd Ed., Pergamon Press: Oxford 1970).
26. Barney CW, Helgeson ME, Valentine MT. Network structure influences bulk modulus of nearly incompressible filled silicone elastomers. Extreme Mechanics Letters. 2022;52, 101616.
27. Jordan JL, Rowland RL, Greenhall J, Moss EK, Huber RC, Willis EC, Hrubiak R, Kenney-Benson C, Bartram B, Sturtevant BT, Elastic properties of polyethylene from high pressure sound speed measurements. Polymer. 2021;212, 123164.
28. Mott PH, Dorgan JR, Roland CM. The bulk modulus and Poisson's ratio of "incompressible" materials. Journal of sound and vibration. 2008;312:572-575.
29. Brillouin L. Diffusion de la lumière et des rayons X par un corps transparent homogène. *Ann Phys (Paris)*. 1922;17:88-122.
30. Blachowicz T, Bukowski R & Kleszczewski Z. Fabry-Perot interferometer in Brillouin scattering experiments. Rev Sci Instrum. 1996;67:4057-4060.
31. Okamoto PR, Rehn LE, Pearson J, Bhadra R, Grimsditch M. Brillouin scattering and transmission electron microscopy studies of radiation-induced elastic softening, disordering and amorphization of intermetallic compounds. *J Less-Common Met*. 1988;140(C):231-244.
32. Lee SA, Lindsay SM, Powell JW, et al. A Brillouin scattering study of the hydration of Li- and Na-DNA films. *Biopolymers*. 1987;26(10):1637-1665
33. Dil JG. Brillouin scattering in condensed matter. Reports Prog Phys. 1982;45(3):285-334.

34. Harley, R., James, D., Miller, A. & White, J. W. Phonons and elastic-moduli of collagen and muscle. Nature. 1977;267, 285–287.
35. Randall, J. & Vaughan, J. M. Brillouin scattering in systems of biological significance. Phil. Trans. R. Soc. Lond. A. 1979;293, 341–348.
36. Lees, S., Tao, N. J. & Lindsay, S. M. Studies of compact hard tissues and collagen by means of Brillouin light-scattering. Connect. Tissue Res. 1990;24, 187–205.
37. Vaughan, J. M. & Randall, J. T. Brillouin scattering, density and elastic properties of the lens and cornea of the eye. Nature. 1980; 284, 489–491.
38. Randall, J. & Vaughan, J. M. The measurement and interpretation of Brillouin scattering in the lens of the eye. Proc. R. Soc. Lond. B. 1982;214, 449–470.
39. Shirasaki M. Virtually Imaged Phased Array. Sci Tech J. 1999;35(1), 113-125.
40. Scarcelli G, Yun SH. Multistage VIPA etalons for high-extinction parallel Brillouin spectroscopy," Opt. Express. 2011;19, 10913-10922.
41. Scarcelli G, Yun SH. Confocal Brillouin microscopy for three-dimensional mechanical imaging. Nat Photonics. 2008;2(1):39-43.
42. Yeung, T., et al. Effects of substrate stiffness on cell morphology, cytoskeletal structure and adhesion. Cell Motility and the Cytoskeleton. 60, 24-34 (2005)
43. Fischer RS, Myers KA, Gardel ML, Waterman CM. Stiffness-controlled three-dimensional extracellular matrices for high-resolution imaging of cell behavior. Nature Protocols, 2012, vol 7, 11, 2056-2066
44. Bedborough, D. S.; Jackson, D. A. Brillouin Scattering Study ofGelatin Gel using a Double Passed Fabry-Perot Spectrometer.Polymer1976,17, 573−576.
45. Zhao, P.; Vanderwal, J. J. Brillouin Scattering Study of GelatinGel.Polym. Gels Networks1997,5,23−36
46. Bailey M, Alunni-Cardinali M, Correa N, Caponi S, Holsgrove T, Barr H, Stone N, Winlove CP, Fioretto D, Palombo F. Viscoelastic properties of biopolymer hydrogels determined by Brillouin spectroscopy: A probe of tissue micromechanics. Sci. Adv. 2020, 6, eabc1937.
47. P.Voudouris, N. Gomopoulos, A. Le Grand, N. Hadjichristidis, G. Floudas, M.D. Ediger, G. Fytas. Does Brillouin light scattering probe the primary glass transition process at temperatures well above glass transition? J. Chem. Phys. 2010, 132(7) ,074906.
48. Wu, P.-J.; Kabakova, I. V.; Ruberti, J. W.; Sherwood, J. M.;Dunlop, I. E.; Paterson, C.; Török, P.; Overby, D. R. Water Content, not Stiffness, Dominates Brillouin Spectroscopy Measurements in Hydrated Materials. Nat. Methods2018,15, 561−562.
49. T. Sakai, M. Kurakazu, Y. Akagi, M. Shibayama & U. Chung. Effect of swelling and deswelling on the elasticity of polymer networks in the dilute to semi-dilute region. Soft Matter, 2012, 8, 2730-2736
50. Del Monte DW, Kim T. Anatomy and physiology of the cornea. J Cataract Refract Surg. 2011;37:588–98.
51. Radner W, Zehetmayer M, Aufreiter R, Mallinger R. Interlacing and cross-angle distribution of collagen lamellae in the human cornea. Cornea 1998; 17;537-543.
52. Maurice DM. The structure and transparency of the cornea. J Physiol. 1957;136:263:286.

53. CoganDG. Applied anatomy and physiology of the cornea. Trans Am Acad Ophtahlmol Otolaryngol. 1951;55:329:359.
54. Muller LJ, Pels E, Schurmans LR, Vrensen GF. A new three-dimensional model of the organization of proteoglycans and collagen fibrils in the human corneal stroma. Exper Eye Resl 2004;78:493-501.
55. Hayashi S, Osawa T, Koujiro T. Comparative observations on corneas, with special reference to bowman's layer and descemet's membrane in mammals and amphibians". Journal of Morphology. 2002;254 (3): 247–58.
56. Sridhar MS. Anatomy of cornea and ocular surface. Indian J Ophthalmol. 2018;66(2):190-194.
57. Chen J, Li Z, Zhang L, et al. Descemet's Membrane Supports Corneal Endothelial Cell Regeneration in Rabbits. Sci Rep. 2017;7(1):1-13.
58. Wilson SE. Bowman's layer in the cornea– structure and function and regeneration. Exp Eye Res. 2020;195:108033.
59. Blackburn BJ, Jenkins MW, Rollins AM, Dupps WJ. A review of structural and biomechanical changes in the cornea in aging, disease, and photochemical crosslinking. Front Bioeng Biotechnol. 2019;7(MAR):66.
60. Roberts, CJ. & Liu, J. Corneal Biomechanics from theory to practice. Kugler Publications. Amsterdam, The Netherlands, 2016.
61. Tuft SJ, Coster DJ. The corneal endothelium. Eye. 1990;4(3):389-424.
62. Merindano Encina, D, Potau, JM, Ruano D, Costa J, Canals M. A comparative study of Bowman's layer in some mammals relationships with other constituent corneal structures. European Journal of Anatomy. 2002;6 (3): 133–40.
63. Polisetti N, Martin G, Cristina Schmitz HR, Schlötzer-Schrehardt U, Schlunck G, Reinhard T. Characterization of Porcine Ocular Surface Epithelial Microenvironment. *International Journal of Molecular Sciences*. 2023; 24(8):7543
64. Rodella U, Bosio L, Ferrari S, Gatto C, Giurgola L, Rossi O, Ciciliot S, Ragazzi E, Ponzin D, D'Amato Tóthová J. Porcine Cornea Storage Ex Vivo Model as an Alternative to Human Donor Tissues for Investigations of Endothelial Layer Preservation. Transl Vis Sci Technol. 2023 3;12(4):24
65. Shoulders MD, Raines RT. Collagen structure and stability. Annu Rev Biochem. 2009;78:929-58.
66. Sayers Z, Koch MH, Whitburn SB, Meek KM, Elliott GF, Harmsen A. Synchrotron x-ray diffraction study of corneal stroma. J. Mol. Biol. 1982;160:593-607
67. Freund DE, McCally RL, Farrell RA, Cristol SM, L'Hernault NL, Edelhauser HF. Ultrastructure in anterior and posterior stroma of perfused human and rabbit corneas. Relation to transparency. IOVS. 1995;36:1508-1523.
68. Turss RFJ, ReimM, Cohlamn CH. Glucose concentration and hydration of the corneal stroma. Ophthalmic Res. 1971;2:7.
69. Muller LJ, Pels E & Vrensen GFJM. The specific architecture of the anterior stroma accounts for maintenance of corneal curvature. J Ophthalmol. 2001;85:437-443.

70. Winkler M, Chai D, Kriling S, et al. Nonlinear Optical Macroscopic Assessment of 3-D Corneal Collagen Organization and Axial Biomechanics. 118 IOVS 2011;52(12):8818.
71. Scarcelli G, Pineda R & Yun SH. Brillouin optical microscopy for corneal biomechanics. IOVS. 2012;53(1):185-190.
72. Petsche SJ, Chernyak D, Martiz J, Levenston ME, Pinsky PM. Depth-dependent transverse shear properties of the human corneal stroma. IOVS. 2012;53(2):873-880.
73. Scarcelli G, Kling S, Quijano E, Pineda R, Marcos S, Yun SH. Brillouin Microscopy of Collagen Crosslinking: Noncontact Depth-Dependent Analysis of Corneal Elastic Modulus. IOVS. 2013;54(2):1418.
74. Wollensak G, Spoerl E, Seiler T. Stress-strain measurements of human and porcine corneas after riboflavin-ultraviolet-Ainduced cross-linking. J Cataract Refract Surg 2003; 29:1780–1785.
75. Puxkandl R, Zizak I, Paris O, et al. Viscoelastic properties of collagen: synchrotron radiation investigations and structural models. Philos Trans R Soc Lond B Biol Sci. 2002;357:191-1967.
76. Misof K, Rapp G, Fratz P. Anew molecular model for collagen elasticity based on synchrotron X-ray scattering evidence. Biophys J. 1997;72: 1376-1381.
77. Fratz P, Misof K, Zizak I, Rapp G, Amenitsch H, Bernstorff S. Fibrillar structure and mechanical properties of collagen. J Struct Biol. 1998;122:119-122.
78. Hatami-Marbini H, Etebu E. An experimental and theoretical analysis of unconfined compression of corneal stroma. J Biomech 2013;46(10):1752-1758.
79. Askeland DR, Fulay PP & Wright WJ. The science and engineering of materials. Cengage Learning. Fifth Edition. Connecticut, USA, 2011.
80. Kim, Ji Hyun, and Joseph Caprioli. “Intraocular Pressure Fluctuation: Is It Important?.” Journal of ophthalmic & vision research vol. 13,2: 170-174 (2018).
81. Khaw PT, Shah P, Elkington AR. Glaucoma--1: diagnosis. BMJ. 2004;328(7431):97-99.
82. Ko MWL, Leung LKK, Lam DCC, Leung CKS. Characterization of corneal tangent modulus in vivo. Acta Ophthalmol. 2013;91(4):263-269.
83. Qian X, Ma T, Shih CC, Heur M, Zhang J, Shung KK, Varma R, Humayun MS, Zhou Q. Ultrasonic Microelastography to Assess Biomechanical Properties of the Cornea. IEEE Trans Biomed Eng. 66(3):647-655 (2019).
84. Roberts, Cynthia J. PhD*; Dupps, William J. Jr. MD, PhD. Biomechanics of corneal ectasia and biomechanical treatments. J Cataract Refract Surg. 2014;40(6):p 991-998
85. Meek KM, Tuft SJ, Huang Y, Gill PS, Hayes S, Newton RH, Bron AJ. Changes in collagen orientation and distribution in keratoconus corneas. Invest Ophthalmol Vis Sci. 2005; 46:19481956.
86. Morishige N, Wahlert AJ, Kenney MC, Brown DJ, Kawamoto K, Chikama T-i, Nishida T, Jester JV. Second-harmonic imaging microscopy of normal human and keratoconus cornea. Invest Ophthalmol Vis Sci. 2007; 48:1087–1094.
87. Hashemi H, Heydarian S, Hooshmand E, Saatchi M, Yekta A, Aghamirsalim M, et al. The Prevalence and risk factors for keratoconus: a systematic review and meta-analysis. Cornea. 2020;39:263–70.

88. Cavas-Martínez, F., De la Cruz Sánchez, E., Nieto Martínez, J. et al. Corneal topography in keratoconus: state of the art. Eye and Vis. 2026;3, 5.
89. Shao P, Eltony AM, Seiler TG, Tavakol B, Pineda R, Koller T Seiler T, Yun SH. Spatially-resolved Brillouin spectroscopy reveals biomechanical changes in early ectatic corneal disease and post-crosslinking in vivo. *Sci Rep*. 2019;9,7467.
90. Vinciguerra R, Ambrósio R, Roberts CJ, Azzolini C, Vinciguerra P. Biomechanical characterization of subclinical keratoconus without topographic or tomographic abnormalities. *J Refract Surg*. 2017;33(6):399-407.
91. Saad A, Lteif Y, Azan E, Gatinel D. Biomechanical properties of keratoconus suspect eyes. *Investig Ophthalmol Vis Sci*. 2010;51(6):2912-2916.
92. Vinciguerra R, Ambrósio R, Elsheikh A, et al. Detection of keratoconus with a new biomechanical index. J Refract Surg. 2016;32(12):803-810.
93. Spörl E, Huhle M, Kasper M, Seiler T. Erhöhung der Festigkeit der Hornhaut durch Vernetzung [Increased rigidity of the cornea caused by intrastromal cross-linking]. Ophthalmologe. 1997 Dec;94(12):902-6.
94. Spörl, E., Huhle, M., Kasper, M. et al. Artificial stiffening of the cornea by induction of intrastromal cross-links. Ophthalmologe. 1997;94, 902–906.
95. Wollensak G, Spoerl E, Seiler T. Riboflavin/ultraviolet-A-induced crosslinking for the treatment of keratoconus. Am J Ophthalmol 2003; 135:620–627.
96. Hedbys BO, Mishima S. The thickness–hydration relationship of the cornea. Exp Eye Res 1966; 5:221–228
97. Holopainen J, Krootila K. Transient Corneal Thinning in eyes Undergoing Corneal Cross-Linking. American Journal of Ophtalmology 2011; 152(4):533-536.
98. Santhiago MR, Randleman JB. The biology of corneal cross-linking derived from ultraviolet light and riboflavin. Exp Eye Res. 2021;202:108355.
99. Angelo L, Gokul-Boptom A, McGhee C, Ziaei M. Corneal Crosslinking: Present and Future. Asia-Pacific Journal of Ophthalmology 2022;11(5):441-452.
100. D.J. Müller, A.C. Dumitru. C. Lo Giudice, H.E. Gaub, P. Hinterdorfer, G. Hummer, J.J. De Yoreo, Y.F. Dufrene, D. Alsteens. Atomic Force Microscopy-Based Force Spectroscopy and Multiparametric Imaging of Biomolecular and Cellular Systems. Chemical Reviews 2021, 121, 19, 11701-11725.
101. B. González-Bermúdez, G.V. Guinea, G.R. Plaza. Advances in Micropipette Aspiration: Applications in Cell Biomechanics, Models, and Extended studies. Biophysical Journal 2019, 116, 587-594.
102. W. Liu, C. Wu. Rheological Study of Soft Matters: A Review of Microrheology and Microrheometers. Macromol. Chem. Phys. 2018, 219, 1022-1352.
103. B.F. Kennedy, P. Wijesinghe, D.D. Sampson. The emergence of optical elastography in biomedicine. Nat. Photonics 2017, 11, 215–221.
104. K. Christensen-Jeffries, O. Couture, P.A. Dayton, Y.C. Eldar, K. Hynynen, F. Kiessling, M. O'Reilly, G.F. Pinton, G. Schmitz, M.X. Tang, M. Tanter, R.J.G van Sloun. Super-resolution Ultrasound Imaging. Ultrasound Med Biol 2020, 46,4, 865-891.

105. Manduca, T.E. Oliphant, M.A. Dresner, J.L. Mahowald, S.A. Kruse, E. Amromin, J.P. Felmlee, J.F. Greenleaf, R.L. Ehman. Magnetic resonance elastography: non-invasive mapping of tissue elasticity. Med. Image Anal. 2011, 5, 4, 237–254.
106. Schroyen, D. Vlassopoulos, P. Van Puyvelde, J. Vermant. Bulk rheometry at high frequencies: a review of experimental approaches. Rheol Acta. 2020, 59:1-22.
107. T. Still, M. Oudich, G. K. Auerhammer, D. Vlassopoulos, B. Djafari-Rouhani, G. Fytas, P. Sheng. Soft silicone rubber in phononic structures: Correct elastic moduli. Phys Rev B 2013, 88, 9: 094-102.
108. D.L. Johnson. J. Elastodynamics of gels. Chem. Phys. 1982, 77, 1531–1539
109. A Bot, RPC Schram, GH Wegdam. Brillouin light scattwering from a biopolymer gel: hypersonic sound waves in gelatin. Colloid Polym. Sci., 1995, 273, 252-256.
110. SC Ng, Y Li. Brillouin light-scattering from polymer gels. J. Phys. II, 1993, 3(8), 1241-1245.
111. T Tanaka, LO Hocker, GB Benedek. Spectrum of light scattered from a viscoelastic gel. J. Chem. Phys., 1973, 59, 5151-5159.
112. SC Ng, TJC Hosea, LM Gran. Determination of the sol-gel transition temperature and phase diagram of a gelation system by Brillouin spectroscopy. J. Phys. E: Sci. Instrum., 1985, 18, 250-252.
113. F Mallamace, N Micali, C Vasi, R Bansil, S Pajevic, F Sciortino. Brillouin scattering from cross-linked gels. J. Phys. II, 1992, 2(12), 2081-2088.
114. C Verdier, PY Longin, M Piau. Dynamic shear and compressional behavior of polydimethylsiloxanes: Ultrasonic and low frequency characterization. Rheol. Acta,1998, 37: 234-244.
115. HH Mitchell, TS Hamilton, FR Steggerda, HW Bean. The chemical composition of the adult human body and its bearing on the biochemistry of growth. J. Biol. Chem, 1945, 158(3), 6225-637.
116. GM Cooper, RE Hausman. The cell: a molecular a pproach. (4th Ed, ASM Press: USA 2007).
117. R.S. Shatat, S.K. Niazi, A. Ariffin,. Synthesis and Characterization of Different Molecular Weights Polyacrylamide. IOSR J. Appl. Chem., 2017, 10, 67-73.
118. Ma, M. Liu, Z. Chen. Preparation and properties of a salt-resistant superabsorbent polymer. J. Appl. Polym. Sci., 2004, 93, 2532-2541.
119. D.S. Janiak, O.B. Ayyub, P. Kofinas. Effects of charge density on the recognition properties of molecularly imprinted polymeric hydrogels. Macromolecules 2004, 42, 1703-1709.
120. C. Zhou, D.E. Heath, A.R. Mohamed-Sharif, S. Rayatpisheh, B.H.L. Oh, X. Rong, R. Beuerman, M.B. Chan-Park. High water content hydrogel with super high refractive index. Macromol. Biosci, 2013, 13, 1485-1491.
121. ILO-WHO International Chemical Safety Cards (ICSCs), “Acrylamide” 2013; https://www.ilo.org/dyn/icsc/showcard.display?p_card_id=0091&p_version=2&p_lang=en.
122. S. Morozova, M. Muthukumar. Elasticity at Swelling Equilibrium of Ultrasoft Polyelectrolyte gels: comparisons of theory and experiments. Macromolecules 2017, 50, 2456-2466.
123. Tsuji, X. Li, M. Shibayama. Evaluation of mesh size in model polymer netwroks consisting of Tetra-ar, and linear poly(ethylene glycol)s. Gels 2018, 4(2),50.

124. M. Rubinstein, R.H. Colby. Polymer Physics. (Oxford University Press 2003).
125. Jia & M. Muthukumar. Interplay between microscopic and macroscopic properties of charged hydrogels. Macromolecules 2020, 53, 90-101.
126. J.E. Mark. Physical properties of polymers handbook (2nd edition. Springer Science 2007).
127. J. Guo, P. André, M. Adam, S. Panyukov, M. Rubenstein, J.M. DeSimone. Solution Properties of Fluorinates Alkyl Methacrylate Polymer in Carbon Dioxide. Macromolecules 2006, 39, 3427-3434.
128. N.R. Richbourg, N.A. Peppas. The swollen polymer network hypothesis: Quantitative models of hydrogel swelling, stiffness, and solute transport. Prog. Polym. Sci., 2020, 105, 101243
129. K.I. Hoshino, T. Nakajima, T. Matsuda, T. Sakai, J.P. Gong. Network elasticity of a model hydrogel as a function of swelling ratio: from shrinking to extreme swelling states. Soft Matter 2018, 14, 9693-9701.
130. B.V. Slaughter, S.S.Khurshid, O.Z. Fisher, A. Khademhosseini, N.A. Peppas. Hydrogels in regenerative medicine. Adv. Mater., 2009, 21(0), 3307-3329.
131. N.R. Richbourg, M.K. Rausch, N.A. Peppas. Cross-evaluation of stiffness measurements methods for hydrogels. Polymer 2022, 258, 125316.
132. L. Brannon-Peppas, N.A. Peppas. Equilibrium swelling behavior of pH-sensitive hydrogels. Chem. Eng. Sci., 1991, 46, 715–722.
133. B.D. Johnson, D.J. Beebe, W.C. Crone. Effects of swelling on the mechanical properties of a pH-sensitive hydrogel for use in microfluidic devices. Mater. Sci. Eng., C, 2004, 24, 575–581.
134. R. Subramani, A. Izquierdo-Alvarez, P. Bhattacharya, M Meerts, P. Moldenaers, H. Ramon, H. Van Oosterwyck. The influence of swelling on elastic properties of polyacrylamide hydrogels. Front. Mater. 2020, 7:212.
135. Shao P, Seiler TG, Eltony AM, et al. Effects of corneal hydration on brillouin microscopy in vivo. Investig Ophthalmol Vis Sci. 2018; 59:3020–3027.
136. Hatami-Marbini H, Etebu E. Hydration dependent biomechanical properties of the corneal stroma. Exp Eye Res. 2013;116:47–54.
137. Hatami-Marbini H, Rahimi A. Stiffening effects of riboflavin/UVA corneal collagen cross-linkingis hydration dependent. J Biomechanics. 2015; 48:1052–1057.
138. Hatami-Marbini H, Rahimi A. Interrelation of hydration, collagen cross-linking treatment, and biomechanical properties of the cornea. Curr Eye Res. 2016; 41:616–622.
139. Hatami-Marbini H, Jayaram SM. Effect of UVA/Riboflavin collagen crosslinking on biomechanics of artificially swollen corneas. IOVS 2018; 59:764-770.
140. Seiler, TG, Shao P, Frueh BE, Yun SH, Seiler T. The influence of hydration on different mechanical moduli of the cornea. Graefes Arch Clin Exp Ophthalmol (2018) 256:1653–1660.
141. Mita, M, Waring GO, Tomita M. High-irradiance accelerated collagen crosslinking for the treatment of keratoconus: Six-month results. J Cataract Refract Surg. 2014: 40(6):1031-1040.
142. Hammer A, Richoz O, Mosquera SA, Tadbibian D, Hoogewoud F, Hafezi F. Corneal Biomechanical Properties at different corneal cross-linking (CXL) irradiances. IOVS. 2014; 55(5):2881.

143. Wernli J, Schumacher S, Spoerl E, Mrochen M. The Efficacy of Corneal Cross-Linking Shows a Sudden Decrease with Very High Intensity UV Light and Short Treatment Time. IOVS 2013; 54(2): 1176-1180.
144. Danielsson M, Parks DM, Boyce MC. Constitutive modeling of porous hyperelastic materials. Mech Mater. 2004; 36:347–358.
145. Gao X, Gu W. A new constitutive model for hydration-dependent mechcanical properties in biological soft tissues and hydrogels. J Biomech 2014; 47(12):3196:3200.
146. Mow VC, Kuei SC, Lai WM, Armstrong CG. Biphasic Creep and Stress-Relaxation of Articular-Cartilage in Compression - Theory and Experiments. J Biomech Eng-T Asme. 1980; 102:73–84.
147. Holz M, Heil SR, Sacco A. Temperature-dependent self-diffusion coefficients of water and six selected molecular liquids for calibration in accurate 1H NMR PFG measurements. Phys Chem Chem Phys. 2000;2(20):4740-4742.
148. Gu WY, Yao H. Effects off hydration and fixed charge density on fluid transport in charged hydrated soft tissues. Annals of biomedical engineering. 2003; 31:1162–1170.
149. Keith Ch, Bird, G, Farmer M. Coherent Backscatter Enhances Reflection Confocal Microscopy. BioTechniques 1998; 25:858-866.
150. Kontadakis GA et al. In vitro effect of corneal collagen cross-linking on corneal hydration properties and stiffness. Graefes Arch Clin Exp Ophthalmol. 2013;251:543-547.
151. Kohlhaas M, Spoerl E, Schilde T, Unger G, Wittig C, Pillunat LE. Biomechanical evidence of the distribution of cross-links in corneas treated with riboflavin and ultraviolet A light. J Cataract Refract Surg 2006; 32:279–283.
152. Bourne W. Clinical estimation of corneal endothelial pump function. TR AM OPHTH SOC. (1998).
153. Ber-Chin Y, Shichijyo S, Matsushige K, Takemura T. Brillouin scattering from PMMA under uniaxial tensile stress. Jpn. J. Appl. Phys. 1982; 21(8):L523-L525.
154. Horiguchi T, Kurashima T, & Tateda M. Tensile strain dependence of Brillouin frequency shift in silica optical fibers. IEEE Photonics Technology Letters. 1989;1(5).
155. Coscetta, A.; Minardo, A.; Zeni, L. Distributed Dynamic Strain Sensing Based on Brillouin Scattering in Optical Fibers. Sensors. 2020; 20,5629.
156. Dong, Yongkang & Teng, Lei & Tong, Peilin & Taofei, Jiang & Zhang, Hongying & Zhu, Tao & Chen, Liang & Bao, Xiaoyi & Lu, Zhiwei. High-sensitivity distributed transverse load sensor with an elliptical-core fiber based on Brillouin dynamic gratings. Optics letters. 2015;40. 5003-5006. 10.1364/OL.40.005003
157. Saxena, Bhayane; Baker, Chams; Bao, Xiaoyi & Chen, Liang. High birefringent Brillouiin frequency shifts in a single-mode As2Se3-PMMA microtaper induced by a transverse load. Optics Letters. 2019;44. 4789-4792.
158. Chen M, Zhang L, Xu J, Chen X, Gu Y, Ren Y, Wang K. Comparability of three intraocular pressure measurement: iCare pro rebound, non-contact and Goldmann applanation tonometry in different IOP group. BMC Ophthalmol. 2019;19(1):225.

159. Qureshi I.A. Intraocular pressure: a comparative analysis in two sexes. Clinical Physiology.1997;17, 247-255.

160. Kling S, Remon L, Pérez-Escudero A, Merayo-Lloves J, & Marcos S. Corneal Biomechanical Changes after Collagen Cross-Linking from Porcine Eye Inflation Experiments. IOVS. 2010;51(8):3961-3968.

161. Pierscionek BK, Asejczyk-Widlicka M, Schachar RA. The effect of changing intraocular pressure on the corneal and scleral curvatures in the fresh porcine eye. Br J Ophthalmol. 200791(6):801-3.

162. Sanchez I, Martin R, Ussa F, Fernandez-Bueno I. The parameters of the porcine eyeball. Graefes Arch Clin Exp Ophthalmol. 2011;249(4):475-82.

163. Shi PJ, Wang IJ, Cai WF & Yen JY. Biomechanical simulation of stress concentration and intraocular pressure in corneas subjected to myopic refractive surgical procedures. Scientific Reports. 2017;7:13906.